CrossMark

ORIGINAL PAPER

Rockburst Generation in Discontinuous Rock Masses

Ben-Guo He[1] · Ravit Zelig[1] · Yossef H. Hatzor[1] · Xia-Ting Feng[2]

Abstract We study rockburst generation in discontinuous rock masses using theoretical and numerical approaches. We begin by developing an analytical solution for the energy change due to tunneling in a continuous rock mass using linear elasticity. We show that the affected zone where most of the increase in elastic strain energy takes place is restricted to an annulus that extends to a distance of three diameters from the tunnel center, regardless of initial tunnel diameter, magnitude of in situ stress, and in situ stress ratio. By considering local elastic strain concentrations, we further delineate the Rockbursting Prone Zone found to be concentrated in an annulus that extends to one diameter from the tunnel center, regardless of original stress ratio, magnitude, and the stiffness of the rock mass. We proceed by arguing that in initially discontinuous rock masses shear stress amplification due to tunneling will inevitably trigger block displacements along preexisting discontinuities much before shear failure of intact rock elements will ensue, because of the lower shear strength of discontinuities with respect to intact rock elements, provided of course that the blocks are removable. We employ the numerical discrete element DDA method to obtain, quantitatively, the kinetic energy, the elastic strain energy, and the dissipated energy in the affected zone in a discontinuous rock due to tunneling. We show that the kinetic energy of ejected blocks due to strain relaxation increases with increasing initial stress and with decreasing frictional resistance of preexisting discontinuities. Finally, we demonstrate how controlled strain energy release by means of top heading and bench excavation methodology can assist in mitigating rockburst hazards due to stain relaxation.

1 Introduction

Rockbursts pose a very serious risk to the safety of deep underground excavations, and yet the underlying mechanism for rockburst generation is still not completely understood. Because of the great risk to workers safety and the extensive damage to equipment, rockbursts are indeed considered by many as the biggest unresolved problem in deep underground excavations. Rockbursts are defined as "a sudden displacement of rock that occurs in the boundary of an excavation, and cause substantial damage to the excavation (Brady and Brown 2006)". Rockbursts may appear as rock slices or rock falls that pop out of the free surface surrounding the excavation, or as violent rock block ejections, all of which are typically accompanied by characteristic acoustic emissions. As of now, two basic mechanisms are discussed in the rock mechanics literatures: (1) strain relaxation due to the formation of new underground space in a highly stressed environment, (2) response to dynamic wave propagation induced by explosions and drilling in which case the source and the damage might be separate in distance and time (Ortlepp and Stacey 1994). Typically, deep excavations can release a large amount of accumulated elastic energy accompanied with

✉ Yossef H. Hatzor
  hatzor@bgu.ac.il

1 Department of Geological and Environmental Sciences, Ben-Gurion University of the Negev, 84105 Beersheva, Israel

2 State Key Laboratory of Geomechanics and Geotechnical Engineering, Institute of Rock and Soil Mechanics, Chinese Academy of Sciences, Wuhan 430071, China

🖆 Springer

intensive dynamic loading (Cook 1966). The stored strain energy in the rock mass cannot be dissipated entirely by shear sliding along joints, and part of the released strain energy may be converted into kinetic energy that leads to strong shock coupled with block ejections.

In the past several decades, vast research related to the causative mechanism of rockbursts has been performed. In situ measurements of rock displacement in deep tunneling projects since the 1960s suggest that the mechanical response of the rock mass in rockburst events is essentially elastic in nature (Mitri 1999). Generally, rockbursts usually fall under one of three classifications: (1) strain burst, (2) pillar burst and (3) fault slip burst (Müller 1991). Any type of rockburst is attributed to some generation mechanism, either self-initiated or triggered remotely. Rockbursts are either mining-induced by energy release causing damage at the source or triggered by significant dynamic stress changes from remote seismic events. In civil works the most common phenomena are referred to as strain bursts, although buckling and face crushing may occur as well (He et al. 2015). As pointed out, rockbursts are a violent failure phenomenon associated with a seismic event, which often occurs in deep, highly stressed ground (Kaiser et al. 1996), the response of which cannot be addressed by static theories of rock behavior. Consequently, a deep insight into the dynamic mechanisms and the application of this knowledge to the excavation and support of underground openings are essential for possible reduction of the risk associated with the rockburst phenomenon (Durrheim et al. 1998). To date, the rockburst phenomenon has been studied in the field using in situ micro seismic monitoring, at the lab using true triaxial tests, and theoretically using analytical and numerical approaches.

In situ monitoring of micro seismicity has been conducted in various projects, in America (Brady and Leighton 1977), South Africa (Ortlepp and Stacey 1994), Canada (Kaiser and Maloney 1997), India (Srinivasan et al. 1997), Australia (Heal 2010) and China (Feng et al. 2015; Lu et al. 2013), in an effort to understand spatial and temporal intensities of rockburst events during underground mining. Interestingly, spatial precursor events were determined a few days before the occurrence of major rockbursts. Moreover, micro seismicity monitoring enabled resolving the moment tensor associated with rockbursting to analyze the shearing mechanism of rockbursts (Cai et al. 2004).

Laboratory dynamic unloading tests under true triaxial conditions were performed to obtain the frequency–amplitude relationship of acoustic emissions resulting from rockbursts of a single rock block (He et al. 2015; Zhao et al. 2014). Analysis of such laboratory induced "strainbursts" in granitic rocks revealed that strain-bursts are nonlinear, dynamic phenomena that occur when a large amount of energy is released towards a pre-existing free face by sliding along pre-existing discontinuities. Through triaxial unloading tests it was found that the unloading elastic modulus is lower than under loading, and that the ultimate strength decreases with the increasing rate of unloading (Huang et al. 2001).

Theoretical study of the rockburst phenomenon focused on energy considerations and indeed some conceptual expressions of the related energy components were proposed and derived for the general case, although consideration of specific parametric variables such as geometry and initial stresses was not attempted (Walsh 1977; Salamon 1984). Numerical methods have also been utilized in the study of rockbursts, primarily with the aim of capturing the precursors for rockbursts to enable development of precautionary measures (Zhu et al. 2010). Various indices, including energy release rate (ERR), excess shear stress (ESS) together with local energy release rate (LERR), have been proposed to analyze the risk associated with rockbursts (Jiang et al. 2010). Continuum approaches have been widely applied in engineering analyses of strainbursts based on static calculations (Zubelewicz and Mróz 1983; Sharan 2007), as well as the distinct element method UDEC with its explicit time integration algorithm (Gu and Ozbay 2014). Using RFPA2D (Rock Failure Process Analysis) it was found that the energy release and micro seismic events tend to increase with increasing rockbursting (Tang and Kaiser 1998). Although these approaches improved our understanding of the rockburst phenomenon, specific evaluation of the various energy components involved in rockburst deformation, i.e., elastic strain energy, kinetic energy of the block system and energy dissipation due to shear sliding along pre-existing discontinuities, has not been proposed to date.

The purpose of this paper is to clarify the physical mechanism of rockburst generation due to strain relaxation in an elastic rock mass, with specific emphasis on the kinetic energy of the block system. The transient release of strain elastic energy triggers rockbursting and therefore its quantitative evaluation will assist in assessing the rockburst potential and its expected magnitude in specific underground conditions, already at the design stage. We derive an analytical solution of energy changes in the surrounding rock mass before and after excavation from first principles of theory of elasticity. We investigate the correlation between energy density concentration and initial principal stress ratio, as well as the effective depth of surrounding rock from newly opening boundary for mitigating rockburst hazard. We validate and employ the numerical, implicit, discrete element discontinuous deformation analysis (DDA) method which is based on the principle of minimum potential energy (Shi 1988), to obtain better understanding of the underlying mechanisms for strain burst generation due to strain relaxation in discontinuous rock masses. For the specific purposes

of this study we use an enhanced version of DDA that incorporates non-reflective boundaries (Bao et al. 2012) and excavation sequence capabilities (Tal et al. 2014). The modified version has been verified using analytical solutions (Bao et al. 2014) as well as field case studies (Hatzor et al. 2015). Ultimately, the combination of the analytical and numerical approaches provides an in-depth understanding of the physical mechanism that controls rockbursts due to strain relaxation both in continuous as well as discontinuous rock masses. Specifically for discontinuous rock masses where ejection of rock blocks is assumed the dominant mechanism, we derive the mutual transformation of the energy components among elastic strain energy, kinetic energy of the entire block system in the Rockbursting Prone Zone (RPZ) and energy dissipation due to shear sliding along pre-existing discontinuities. We investigate the influence of frictional resistance and in situ stress on the intensity of rockbursting so that we can now identify the conditions at which violent rockbursts are most likely to occur in a discontinuous, relatively stiff, rock mass. An important mitigating measure would be the release of stored strain energy where the potential for rockbursts is high (Xu et al. 2015). An example of rockburst mitigation using top heading distressing in comparison with full-face excavation is demonstrated using the Jinping hydroelectric project as a case study.

2 The Affected Area and the Rockbursting Prone Zone Based on Energy Considerations

It is generally accepted that rockbursts are a manifestation of rapid release of a large amount of elastic energy stored in the rock mass. Therefore, inspection of the energy change due to tunneling in highly stressed environments can provide a meaningful insight into the mechanics of rockbursts. Below we derive analytical expressions for the change in elastic strain energy and for the energy concentration ratio due to

2.1 Energy Change Due to Excavation

We consider a semi-infinite underground space subjected to initial far field stresses under plane-strain conditions (see Fig. 1) assuming for now a continuous linear elastic rock mass. To enable clarifying the strain energy budget due to tunneling, no support is considered hereinafter and body forces are ignored. The sign convention used throughout this paper is that compressive stresses and strains are positive.

Assuming σ_x^o, σ_y^o, and σ_z^o are principal stresses under plane-strain, the shear stresses in the cross-sectional planes are zero ($\tau_{yz}^o = \tau_{zx}^o = \tau_{xy}^o = 0$). The elastic strain energy in the initial state before the excavation can be expressed as (see also Fig. 2):

$$U_{A,B}^o = \varphi^o \times S_{A,B}$$
$$= \frac{1+v}{2E}\left[(1-v)(\sigma_x^o + \sigma_y^o)^2 - 2\sigma_x^o\sigma_y^o\right] \times S_{A,B} \qquad (1)$$

were the complete derivation of Eq. (1) is provided in the "Appendix".

To help demonstrate our approach we will use quantitative examples as we go along. Let us consider a linear elastic rock with $v = 0.22$ and $E = 25.3$ GPa, subjected to initial stresses of $\sigma_x^o = 60$ MPa, and $\sigma_y^o = 30$ MPa. Assuming plane-strain, by means of Eq. (1) the strain energy density of unit volume before the excavation is:

$$\varphi^o = \frac{1+0.22}{2 \times 25.3 \times 10^9}[(1-0.22) \times (60,000,000$$
$$+ 30,000,000)^2 - 2 \times 60,000,000 \times 30,000,000]$$
$$= 65,532.81 \ (\text{J m}^{-3})$$

Let the tunnel shown in Fig. 1b have radius $a = 4$ m and let the analyzed domain extend to a radius $b = 12$ m. The total elastic strain energy in the initial state (before the excavation) is found by superposition:

$$\begin{cases} U_A^o = \int\limits_{S_A} \varphi^o \mathrm{d}S = \int_0^a \int_0^{2\pi} \varphi^o r\mathrm{d}\theta\mathrm{d}r = \int_0^4 \int_0^{2\pi} 65,532.81 \times r\mathrm{d}\theta\mathrm{d}r = 32,94,038 \ (\text{J}) \\ U_B^o = \int\limits_{S_B} \varphi^o \mathrm{d}S = \int_a^b \int_0^{2\pi} \varphi^o r\mathrm{d}\theta\mathrm{d}r = \int_4^{12} \int_0^{2\pi} 65,532.81 \times r\mathrm{d}\theta\mathrm{d}r = 26,352,310 \ (\text{J}) \\ U^o = U_A^o + U_B^o = 29,646,348 \ (\text{J}) \end{cases} \qquad (2)$$

tunneling using linear elasticity. These analytical expressions are used to delineate the affected area due to tunneling and the zone most likely to generate rockbursts, the "Rockbursting Prone Zone" (RPZ).

It can be shown (for complete derivation see "Appendix") that the total elastic strain energy stored in an annulus S_B around a circular opening after the excavation (see Fig. 2) may be expressed as:

Fig. 1 Stresses around a circular opening: circular opening radius of a and external research domain radius of b: **a** three-dimensional sign convention; **b** schematic diagram of analyzed domain. Note that per unit length of the tunnel is considered here assuming plane strain
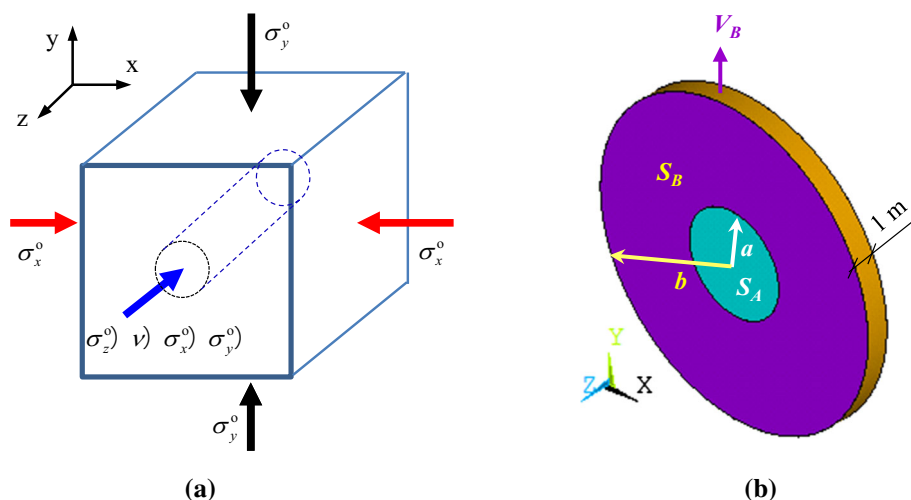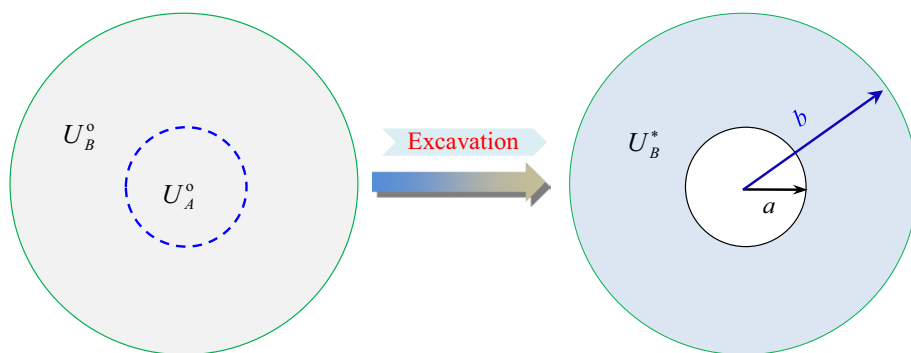

(a)

(b)

Fig. 2 Scheme of excavation-induced energy of surrounding rock

$$U_B^* = \frac{\pi}{E}\left\{(1-v^2)\int_a^b\left[\left(\sigma_x^o+\sigma_y^o\right)^2 r+2\left(\sigma_x^o-\sigma_y^o\right)^2\frac{a^4}{r^3}\right]dr\right.$$

$$+2(1+v)\int_a^b\left[\frac{\left(\sigma_x^o+\sigma_y^o\right)^2}{4}\frac{a^4}{r^3}+\frac{\left(\sigma_x^o-\sigma_y^o\right)^2 a^4}{4}\right.$$

$$\left.\times\left(\frac{2}{r^3}-\frac{12a^2}{r^5}+\frac{9a^4}{r^7}\right)-\sigma_x^o\sigma_y^o r dr\right]\right\}$$

$$=\frac{\pi}{E}\left\{(1+v^2)\left[\frac{1}{2}\left(\sigma_x^o+\sigma_y^o\right)^2 r^2\Big|_a^b-\left(\sigma_x^o-\sigma_y^o\right)^2 a^4\frac{1}{r^2}\Big|_a^b\right]\right.$$

$$+2(1+v)\left[-\frac{\left(\sigma_x^o+\sigma_y^o\right)^2}{8}a^4\frac{1}{r^2}\Big|_a^b+\frac{\left(\sigma_x^o-\sigma_y^o\right)^2 a^4}{4}\right.$$

$$\left.\left.\times\left(-\frac{1}{r^2}\Big|_a^b+3a^2\frac{1}{r^4}\Big|_a^b-\frac{3}{2}a^4\frac{1}{r^6}\Big|_a^b\right)-\frac{\sigma_x^o\sigma_y^o}{2}r^2\Big|_a^b\right]\right\}$$

(3)

With the parameters used in the previous example, the total elastic strain energy stored in annulus S_B after excavation by means of Eq. (3) is $U_B^* = 31{,}599{,}350$ J whereas before the excavation we get $U_A^o = 3{,}294{,}038$ J,

$U_B^o = 26{,}352{,}310$ J (see Eq. (2)). The relative energy changes due to the excavation for this particular example can be expressed using the following expressions:

$$\frac{U_B^*-U_B^o}{U_B^o}\times100\ \% = 19.911\ \%$$

$$\frac{U_B^*-U_B^o}{U_A^o}\times100\ \% = 159.29\ \%$$

(4)

The term $\left(U_B^*-U_B^o\right)/U_B^o$ scales the energy change in the annulus with respect to the original annulus energy. It will decrease with increasing domain boundary (b) and will tend to zero at infinity. The term $\left(U_B^*-U_B^o\right)/U_A^o$ scales the energy change in the annulus with respect to the energy of the tunnel before excavation. It will therefore increase with increasing domain boundary (b) until it will reach some constant value at infinity (see Table 1). Note that the mechanical stiffness of the rock mass, as scaled by the Young's modulus, does not influence these ratios [see Eq. (4)].

To summarize this section, it now becomes apparent that two factors directly influence the amount of strain energy that will be concentrated in the rock mass following the excavation, thus increasing the risk for instantaneous

Table 1 Strain energy change with increasing analyzed domain boundary (tunnel diameter $D = 8$ m)

Analyzed domain radius b (m)	6 m (0.75D)	8 m (1D)	12 m (1.5D)	24 m (3D)	800 m (100D)
Initial energy of annulus S_B (U_B^o /kJ)	4118	9882	26,352	115,291	131,758,200
Excavation-induced energy of annulus S_B (U_B^* /kJ)	7262	14,200	31,599	121,144	131,764,300
$\dfrac{U_B^* - U_B^o}{U_B^o} \times 100$ %	76.374↑	43.698↑	19.911↑	5.077↑	0.0046↑
$\dfrac{U_B^* - U_B^o}{U_A^o} \times 100$ %	95.468↑	131.095↑	159.290↑	177.688↑	184.100↑

D is the diameter of the circular opening, as 2 times radius a. b represents the distance from the tunnel center and analyzed domain radius $b = 100D$ can be deemed as infinity

energy release in the affected zone: (1) tunnel diameter, (2) level of initial in situ stress.

2.2 Redistribution of Energy Density

Excavation of underground space is typically followed by radial stress relaxation during which some of the stored elastic strain energy in the rock mass surrounding the excavation is released. The radial deformation into the newly formed space is coupled by tangential stress concentration near the opening [see Eq. (18)], leading to energy concentration at localized positions around the opening. We investigate here the influence of opening diameter and initial stress magnitude on energy concentrations around the opening, in order to enable a quantitative discussion of excavation induced rockbursting. To that end, we use again the energy increase ratio $(U_B^* - U_B^o)/U_A^o$ as defined above, to scale the energy change in the annulus with respect to the energy of the initial tunnel before excavation. Results pertaining to three different scenarios are presented in Table 2. Inspection of the results of this analysis reveals that most of the energy increase is concentrated in an annulus extended to a distance of three times the opening diameter, regardless of variables such as the opening diameter, the magnitude of the initial stresses and the initial principal stress ratio. To appreciate this note that up to an annulus distance of $3D$ (D is the diameter of the circular opening) the energy increase ratio is approximately 1.7, beyond which the increase is negligible. Since the same results are obtained for the three possible cases, including various opening diameters and initial principal stresses, we conclude that the affected area due to

tunneling generally extends to a distance of three diameters from the tunnel center.

To study the influence of principal stress ratio on local energy density concentrations within the affected area we use an "energy density concentration index", defined here as: ϕ^*/ϕ^o. This index provides the ratio between energy densities before and after the excavation, thus scaling the increase in strain energy due to the excavation (see Fig. 3). Although the energy increase ratio $(U_B^* - U_B^o)/U_A^o$ remains 1.7 inside the affected area to a distance of $3D$, regardless of tunnel diameter and initial stress ratio (Table 2), the energy density concentration indices ϕ^*/ϕ^o at different localities in the affected area are distinctly different. The maximum energy density is parallel to the major far field principal stress, in this particular case at the roof under initial principal stress ratio $k = \sigma_1/\sigma_2 = 2$. The index ϕ^*/ϕ^o drops from extremely high-energy density concentration ratio of 6.46 at the roof to as little as 0.26 at the sidewall (see Fig. 3a), a difference of 25 times! These great differences in energy density concentrations must lead to inhomogeneous release of strain energy around the opening boundary. At a distance of one fourth of the opening diameter, a more homogenous redistribution of energy density ratio is obtained, from a ratio of 2.09 above the roof to 0.48 behind the sidewall. As would be intuitively expected, under an initially hydrostatic stress regime (see Fig. 3b) the energy redistribution is homogenous and decreases from a ratio of 2.79 at the immediate face to 1.35 at one fourth of the tunnel diameter.

The variations in strain energy densities with distance from the tunnel boundary in two orthogonal directions parallel to the principal axes (see Fig. 4) are plotted in

Table 2 Energy increase ratios $(U_B^* - U_B^o)/U_A^o$ in annulus S_B for different initial stresses, tunnel radius (a), and domain boundary (b)

Case no.	Initial principal stress (MPa)			Excavation radius a (m)	Analyzed domain radius b (m)				
	σ_x^o	σ_y^o	$k = \sigma_x^o/\sigma_y^o$		0.75D (%)	1D (%)	1.5D (%)	3D (%)	100D (%)
No. 1	60	30	2	4	95.47	131.11	159.29	177.69	184.10
No. 2	10	5	2	6					
No. 3	30	30	1	4	99.21	133.93	158.73	173.61	178.57

Fig. 3 Energy density concentration index (ϕ^*/ϕ°) at opening boundary (*solid line*) and at a distance of one fourth of the opening diameter (*dashed line*) for principal stress ratio: **a** $k = 2$; **b** $k = 1$. Note that ϕ^*/ϕ° is defined as the ratio between energy densities pre and post excavation states, to scale the increase of strain energy due to excavation. Here D is the diameter of the excavation
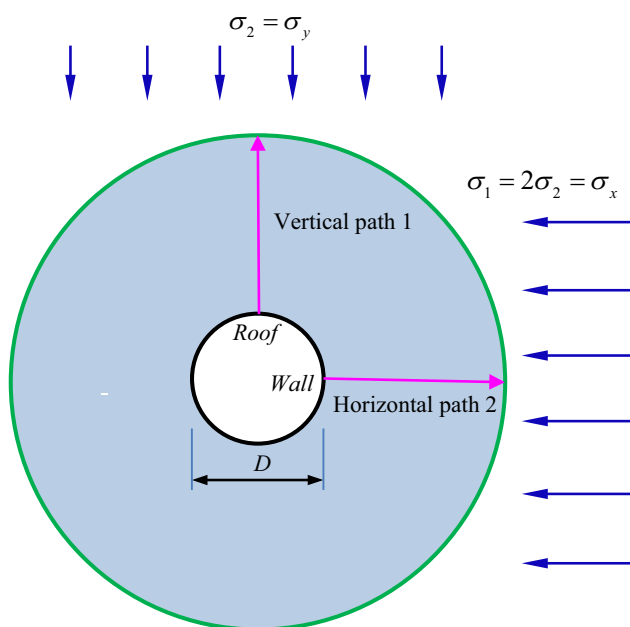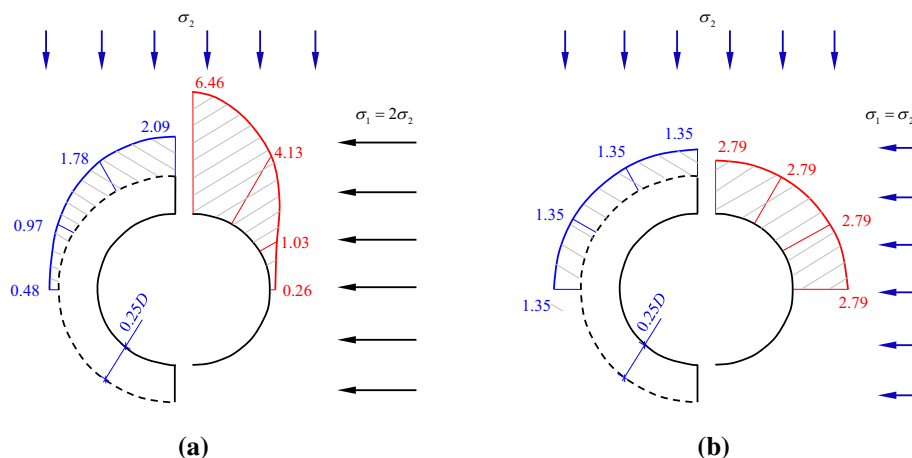

Fig. 4 Scheme of two measurement paths in two orthogonal directions parallel to the principal axis

Fig. 5 Distribution of strain energy density concentration index (ϕ^*/ϕ°) parallel to the principal axis in annulus around boundary subjected to various in situ principal stress ratios: **a** $k = 2$; **b** $k = 1$. Note that the energy density concentration is homogenous around the opening under hydrostatic stress regime of $k = 1$

Fig. 5. For an initial principal stress ratio of $k = 2$ (Fig. 5a), because the initial horizontal stress ($\sigma_1 = \sigma_x$) is twice the initial vertical stress ($\sigma_2 = \sigma_y$), the energy density concentration index at the roof is much higher than that at the sidewall, as would be expected considering stress concentrations around a circular cavity as provided by Kirsch solution. For a hydrostatic pressure of $k = 1$ (Fig. 5b), the energy density concentration index is homogenous around the opening: 2.79. It is apparent from inspection of the results shown in Fig. 5 that most of the strain energy increase is restricted to an annulus thickness of roughly $0.5D$ outside the tunnel boundary, namely from $0.5D$ (at the opening boundary) to $1.0D$. Therefore, an annulus of $0.5D$ thickness from a newly opening boundary
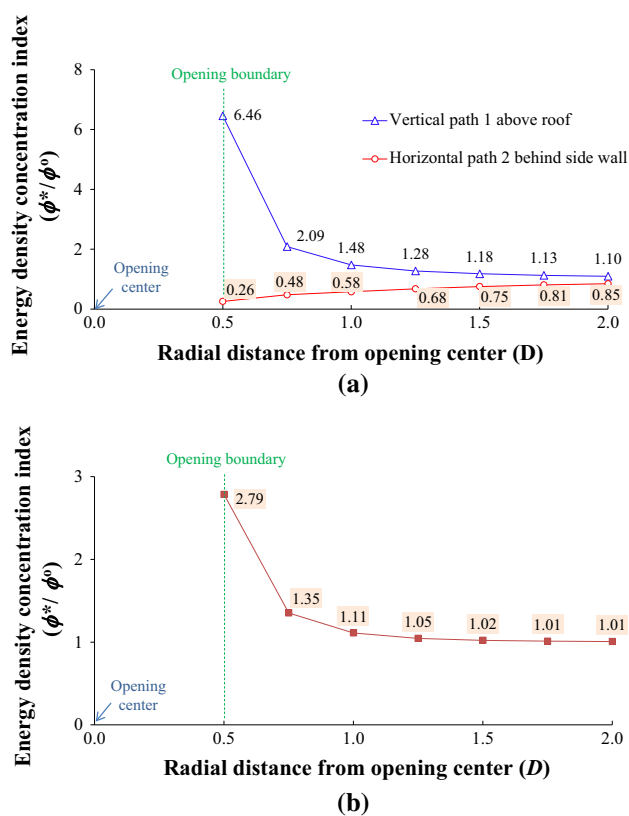
is expected to generate most rockbursting activity. This annulus is considered as the effective depth to be utilized for alleviating rockbursts by measures such as distressing boreholes, top heading excavations, or rock bolting reinforcement. At a distance greater than $1D$ from new opening boundaries the energy density increase is negligible. We therefore hereby define the Rockbursting Prone Zone
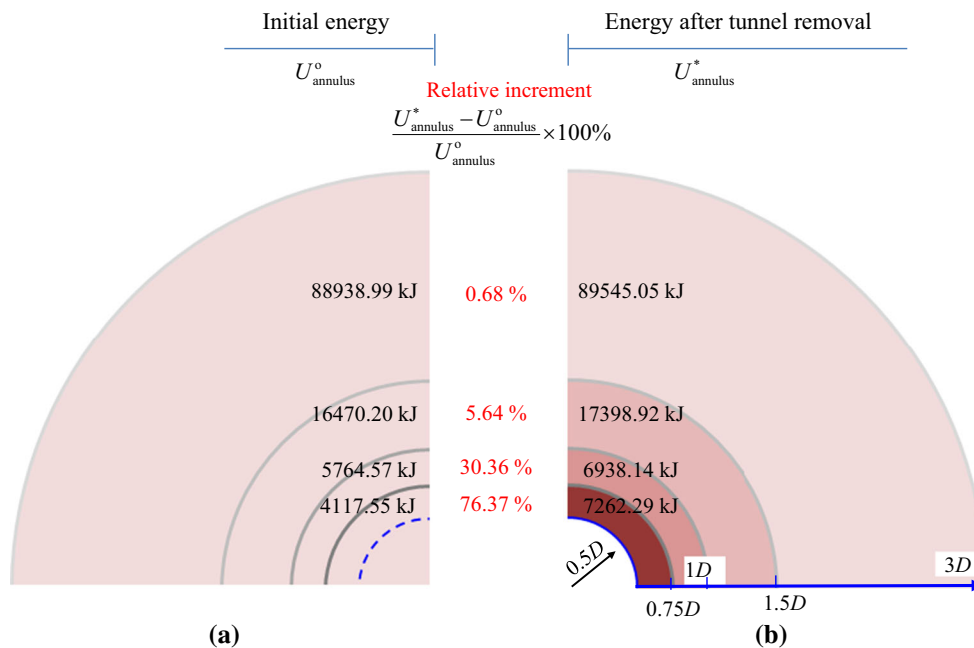
Fig. 6 Relative increment rate of strain energy stored in every annulus around the circular excavation: **a** initial undisturbed state; **b** concentration of energy density due to excavation. Note that the notation U represents stored energy in four annuluses, i.e., the radii of which are from 0.5D to 0.75D, from 0.75D to 1D, from 1D to 1.5D and from 1.5D to 3D on the x-axis, respectively. Here 0.5D represents the newly opening boundary

(RPZ) as an annulus around a circular excavation that extends to a distance of one diameter from the center of the opening, regardless of initial tunnel diameter, initial in situ stress level, and initial tress ratio.

2.3 Local Energy Concentrations Within the RPZ

Probing further into the RPZ as defined above, it is instructive to consider the distribution of stored strain energy in concentric increments around the tunnel, as shown in Fig. 6 for a tunnel diameter of $D = 8$ m and principal stress ratio of $k = 2$. In an annulus between 0.5D and 0.75D measured from the tunnel center the relative incremental increase in strain energy is 76.37 % and it drops to 30.36 % in annulus between 0.75D and 1.0D at the boundary of the RPZ. In annulus between 1.0D and 1.5D the energy increase ratio drops further to 5.64 %. This analysis further confirms our conclusion that the RPZ extends to a distance of one diameter from the tunnel center, in an annulus between 0.5D and 1.0D, measured from the tunnel center. This conclusion, which is obtained here theoretically, is supported by observations performed by Panthi (2012) who measured the rockburst depth impact in a tunnel in the Himalayas and suggested that the impact depth depends on the tangential stress and the particular characteristics of the rock mass. Moreover, extensive field observations performed during tunneling of the Jinping headrace tunnels (Shan and Yan 2010) suggest that most rockbursting activity occurs after the working face has advanced between 6 and 12 m, which in this case roughly corresponds to 0.5D–1D, the rockbursting prone zone as defined in this paper.

3 Numerical Modeling of P-Wave Propagation in Discontinuous Rocks

3.1 The Relevance of Discontinuous Analysis in Rockburst Research

Once the excavation is created, stress redistribution will take place where tangential stress (i.e., major principal stress σ_1) increases while radial stress (the minimum principal stress σ_3) decreases to zero, resulting in the development of maximum shear stress, i.e., $\tau = (\sigma_1 - \sigma_3)/2$, at the newly created opening boundary. Where and when the maximum shear stress exceeds the frictional resistance of pre-existing joints, instantaneous sliding will occur provided that the blocks are finite and removable, consequently emitting strong seismic waves, which will propagate through the discontinuous rock mass. Such an event may be considered as a rockburst generated by slip of removable blocks along pre-existing discontinuities. We argue that since the shear strength of pre-existing discontinuities is much lower than the shear strength of intact rock elements, it is much more likely that at critical

locations around the tunnel boundary the increased shear stress will exceed the level of available discontinuity shear strength before it will approach the level of shear strength of intact rock elements. Therefore, rockbursts due to dynamic ejection of blocks in the process of strain relaxation are much more likely in discontinuous rock masses than rockbursts due to fracturing of intact rock elements.

This rationale provides the motivation to focus the numerical analysis in this study on discrete element methods, and we choose to do this with the numerical, implicit, DDA method (Shi 1993). In this section, the capability of DDA to model accurately burst induced P-wave propagation is first validated, using results from a real case study. In the next section, DDA is used to study the energy components of rockburst deformation in discontinuous rock masses.

In this paper, we use two enhancements recently introduced to improve DDA modeling capabilities of dynamic deformation in the context of deep underground excavations: (1) introduction of non-reflective boundaries (Bao et al. 2012) the essentials of which are briefly reviewed below, and (2) introduction of sequential excavation (Tal et al. 2014).

3.2 Implementation of Non-reflective Boundaries in DDA

The non-reflective boundary enhancement proposed by Bao et al. (2012) involves dampers in the normal and tangential directions, which incorporate the block velocities:

$$\begin{cases} f_n = -\rho c_p v_n \\ f_s = -\rho c_s v_s \end{cases} \tag{5}$$

where ρ is material density; c_p and c_s are the characteristic propagation velocities of P- and S-waves in the material; v_n and v_s are the normal and tangential velocities of the boundary block. From elastic wave propagation theory the characteristic P- and S-wave velocities for the material are:

$$c_p = \sqrt{\frac{E(1-v)}{\rho(1+v)(1-2v)}} \tag{6}$$

$$c_s = \sqrt{\frac{E}{\rho(1+v)}} \tag{7}$$

where E and v are the material's Young's modulus and Poisson's ratio.

The normal and tangential particle velocities of the boundary in cartesian coordinates can be obtained by the following relationships:

$$\begin{cases} v_n = v_x \sin \alpha - v_y \cos \alpha \\ v_t = v_x \cos \alpha + v_y \sin \alpha \end{cases} \tag{8}$$

where α is the direction angle of the boundary edge corresponding to the x-axis; v_x and v_y are the particle velocities in the x and y directions, respectively.

3.3 Numerical Model Validation and Calibration

Research performed during construction of the Jinping hydroelectric station is used here as a case study for numerical model calibration and validation. Many rockbursts have been recorded and documented during the excavation of seven, 17 km long, parallel tunnels connecting between Jinping I and Jinping II hydropower stations, advanced under a maximum overburden of 2525 m (Wang et al. 2012). The tunnels were mostly excavated in marble (Wu et al. 2010). A high-performance integrated seismic system was employed in the tunnels by Feng et al. (2015) for rockburst monitoring and warning in order to reduce the associated rockburst risk and ensure workers safety and smooth construction operations. Adjacent sensors in the axial direction along the tunnel were labeled a "group" where the qth group of sensors were denoted by $S_{q1}, \ldots, S_{qn}$ (see Fig. 7). The field-test layout as shown in Fig. 8a was modeled with DDA using the mesh shown in Fig. 8b.
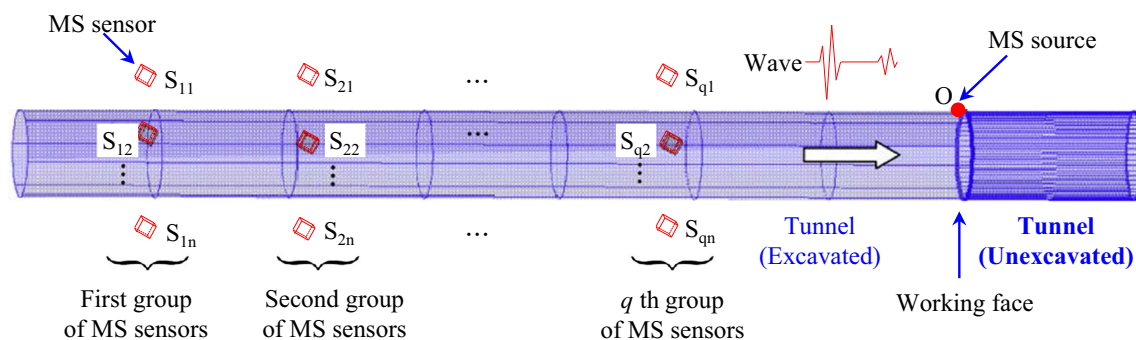

Fig. 7 Diagram showing MS monitoring in Jinping drainage tunnel (modified after Feng et al. 2015). Microseismic event labeled O
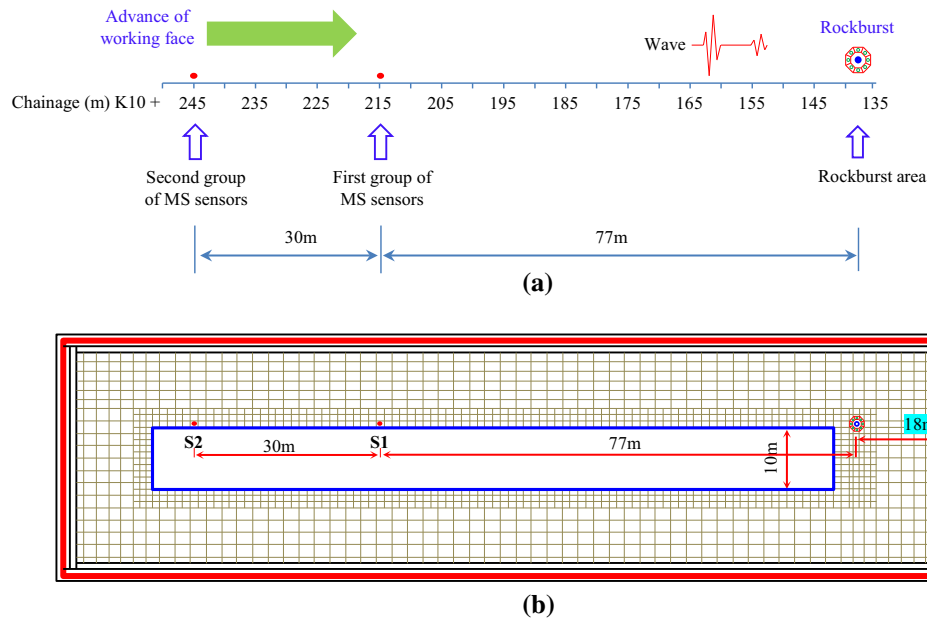
Fig. 8 Configuration of blasting source and monitoring points: **a** field-test layout of microseismic sensors (data from Feng et al. 2015); **b** DDA mesh with non-reflective boundaries (*red boundary lines*) (color figure online)

To simulate a blasting source with DDA, loading points were positioned at the centroids of eight octagonal shaped blocks, each of 1 m width (see Fig. 9). Each loading point was loaded with a pressure time history function of the following form (Drake et al. 1989):

$$P_{\mathrm{t}} = P_0 \cdot e^{\frac{-(t-1.1t_{\mathrm{a}})}{t_{\mathrm{a}}}} \tag{9}$$

where P_{t} and P_0 are shock stress at time t and peak shock stress, respectively. Note that t is the elapsed time from blasting at the source and t_{a} is the arrival time to distance R where $t_{\mathrm{a}} = R/c$ and c is the characteristic P-wave velocity of the material. We use a peak force in this simulation of 10,000 kN, resulting in normally incident peak stress of 10 MPa at the edges of the octagonal load elements. The mechanical parameters for the material used in the simulation are Young's modulus $E = 25.3$ GPa, Poisson's ratio $v = 0.22$, initial cohesion 23.9 MPa and tensile strength 1.5 MPa, following measurements performed in the field (Li et al. 2012). The Mohr–Coulomb failure criterion is applied to model shear sliding along pre-discontinuities in DDA, a discontinuity friction angle of 46° is assumed here for all discontinuities. Viscous boundaries as reviewed above are employed in the DDA simulations to avoid artificial reflections from the boundaries that may obscure the results of the simulation. The time step size is set at 10^{-5} s which, based on our experience (Zelig et al. 2015), should minimize numeric errors in the given configuration. The results of the validation study are shown in

Fig. 10. In Fig. 10a, b the DDA time histories for monitoring stations S1 and S2 are shown. The theoretical arrival times at each point, as obtained from the material properties used [Eq. (6)] are plotted as red solid triangles and indeed, an excellent agreement is obtained between DDA and the theoretical arrival times at each station. The actual arrivals as measured in the field in each station are plotted as (*) and they are clearly much earlier than obtained either numerically, or theoretically. We believe the discrepancy is due to difference in material properties between the assumed for numerical or theoretical computations and the actually encountered values in the field near the face. Indeed, the rock mass parameters quoted and used in our analysis were not measured between chainage K10 + 245-K + 135 where the validation study is performed, but in test tunnels between stations K08 + 680 to K08 + 750 (Li et al. 2012) where similar rock mass conditions and rockbursts were encountered.

In Fig. 10c time histories measured near the right boundary are plotted along with the theoretically calculated arrival times using Eq. (6). Again, a very good agreement is obtained between DDA and the theoretical values. Moreover, the time histories plotted in Fig. 10c demonstrate very clearly the efficiency of the viscous boundary used, as no reflections are obtained with DDA at all. This absorbing capacity of the viscous boundaries enables accurate representation of an infinite medium using a finite analyzed domain in further simulations.
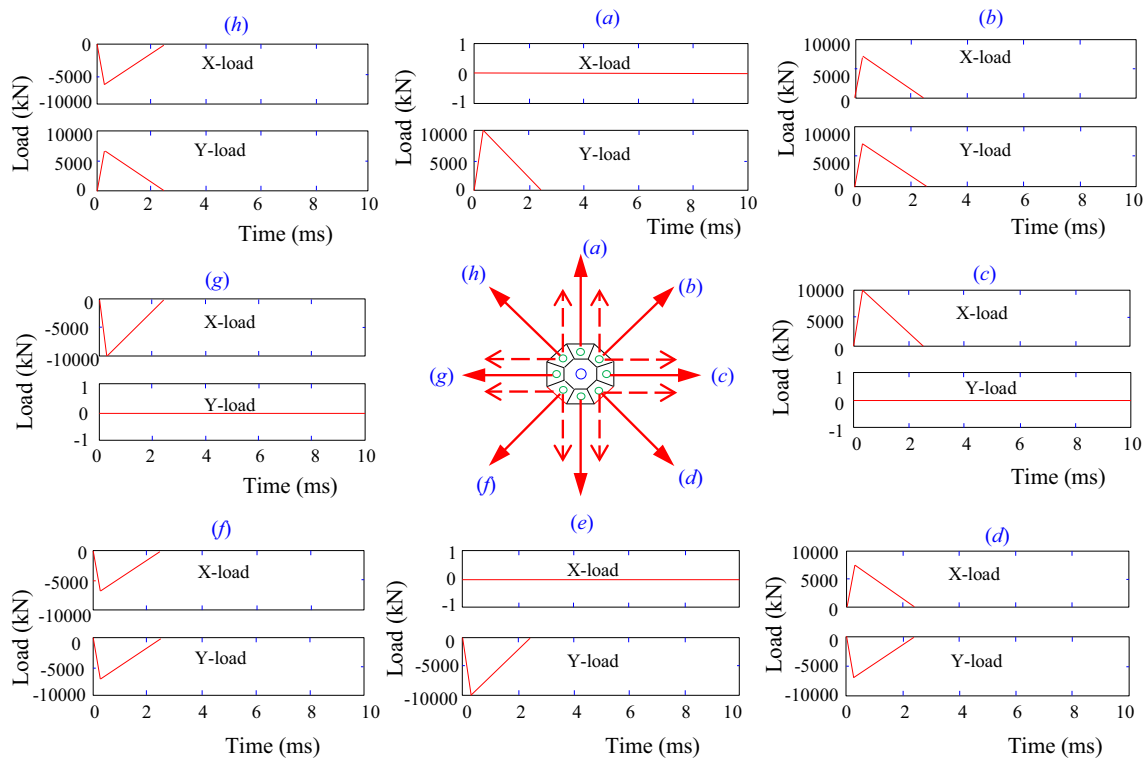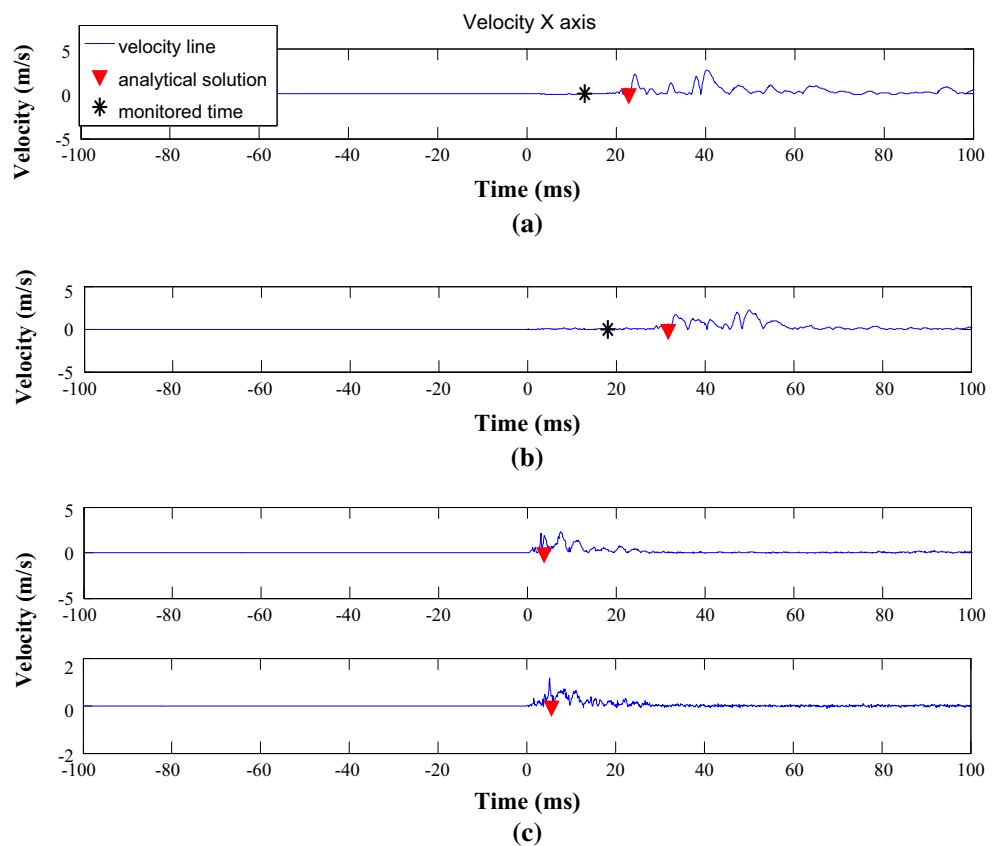
Fig. 9 *P*-wave load function in eight directions versus time imposed at blasting source

Fig. 10 *P*-wave velocities in horizontal direction as a function of elapsed time from blast in discontinuations rock masses with respect to analytical solution and on-site monitoring: **a** S1 monitoring point; **b** S2 monitoring point; **c** control measurement points on right boundary block with non-reflective boundaries (color figure online)

4 Rockburst Energy Distribution in a Discontinuous Rock Mass

4.1 Modeling Deformation of the Affected Area with DDA

We have shown that the increase in energy in the affected area, to a distance of $3D$ from the tunnel center, amounted to 170 % more than the originally stored energy. This energy increase must be balanced, once the excavation is formed, by three energy components in the block system as shown in Eq. (10):

$$U_B^o + 1.7 \times U_A^o = U_{e,B}^* + U_{k,B}^* + U_{d,B}^* \quad (10)$$

where $U_{e,B}^*$ = strain energy stored in the rock blocks, $U_{k,B}^*$ = kinetic energy of the block system, $U_{d,B}^*$ = dissipated energy due to frictional sliding along pre-existing discontinuities.

Before we proceed any further it should be pointed out that the DDA method (Shi 1993) is formulated in plane stress whereas our analytical approach assumes plain strain conditions. It can easily be shown that under plane strain $\sigma_z = v(\sigma_x + \sigma_y)$. Inserting this special case into the general form of the constitutive law (Eq. (13) in Appendix), the two-dimensional strain components under plane strain conditions are:

$$\begin{cases} \varepsilon_x = \dfrac{1-v^2}{E}\left(\sigma_x - \dfrac{v}{1-v}\sigma_y\right) \\ \varepsilon_y = \dfrac{1-v^2}{E}\left(\sigma_y - \dfrac{v}{1-v}\sigma_x\right) \\ \gamma_{xy} = \dfrac{2(1+v)}{E}\tau_{xy} \end{cases} \quad (11)$$

Therefore, if the values of E and v in DDA are replaced with $\frac{E}{1-v^2}$ and $\frac{v}{1-v}$, DDA in its plane stress formulation can be applied for plane strain conditions, without any further modifications.

We impose in situ stresses before the tunnel is removed, and forward DDA modeling is performed under no gravity as body forces are also ignored in the development of our

analytical expression for the energy increase due to tunneling. The following elastic parameters are assumed for the rock mass: material density $\rho = 2563$ kg/m^3, Young's Modulus $E = 25.3$ GPa and Poisson's ratio $v = 0.22$. Two inclined intersecting joint sets are considered in this two dimensional simulation dipping 45° to the left and 30° to the right of the cross section, with spacing of 5 m (see Fig. 11a).

The changes in energy components in the affected area are computed as a function of time for different values of discontinuity friction and stress. 70 blocks comprise the affected area (dashed circle in Fig. 11b) the deformation of which is computed by DDA at measurement points that are positioned at the centroid of the each one of the 70 blocks.

4.2 Influence of Frictional Resistance on Rockburst Energy

The evolution of the shock wave with time as expressed in terms of the kinetic energy of the block system as obtained with DDA is shown in Fig. 12 for a discontinuous medium subjected to principal stress magnitudes of $\sigma_1 = \sigma_x = 60$ MPa, $\sigma_2 = \sigma_y = 30$ MPa acting in the horizontal and vertical directions, respectively. Using the sequential excavation enhancement to DDA (Tal et al. 2014) the opening is created 0.3 s after the beginning of the simulation. The kinetic energy of the block system rises dramatically once the excavation is created. A peak value of instantaneous kinetic energy is attained very rapidly, approximately 0.0028 s after the excavation is created, and it drops rapidly 0.006 s after the peak. Eventually, the kinetic energy of the system attains a constant value, corresponding to the kinetic energy of the single ejected key block (recall that no gravity is applied and therefore the ejected block maintains a constant kinetic energy).

The kinetic energy of the block system in the affected area can be obtained by summing the kinetic energies of all the individual blocks in the affected area: $U_{k,B}^* = \sum_{i=1}^{70} \frac{1}{2}mv_i^2$, the velocities of which are recorded at
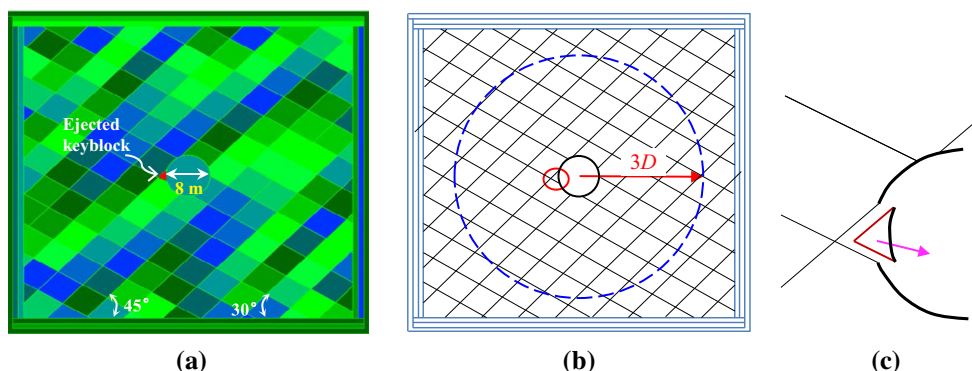

Fig. 11 A two dimensional model utilizing modified version of DDA: **a** blocky rock mass system; **b** analyzed domain; **c** ejected key block
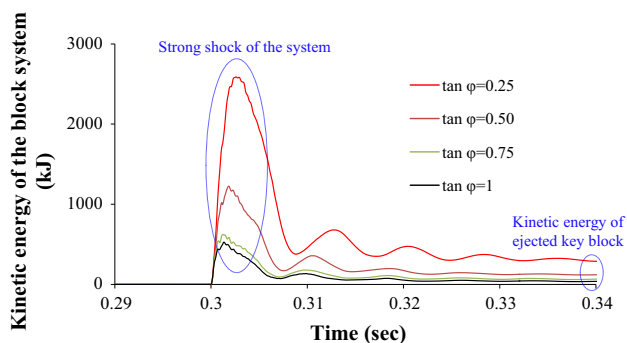
Fig. 12 Evolution of instantaneous kinetic energy of the block system with various friction coefficients. Note that the opening is created at time of 0.3 s represented on horizontal axis using modified DDA with excavation sequence capacities

measurement points that are positioned at the centroid of the each one of the 70 blocks in the DDA mesh. Block stresses are also recorded at the same measurement points and are used to compute the elastic strain energy of the each one of the 70 blocks so that the total elastic strain energy of the affected area may be computed as: $U_{e,B}^* = \sum_{i=1}^{70} \phi_i A_i$. From a viewpoint of energy transformation, both the strain and kinetic energies are recoverable and can be transferred to other forms of energy components, whereas the dissipated energy, here mainly due to shear displacement along discontinuities, is not recoverable. The difference between the total energy at time of excavation and the recoverable energy components during rockbursting is the dissipated energy which can be determined using Eq. (10).

The various energy components as obtained with DDA using Eq. (10) are plotted in Fig. 13 as a function of discontinuity friction. Inspection of Fig. 13 reveals that friction plays an important role in rearrangement of energy components, especially the instantaneous kinetic energy of the block system (red line in Fig. 13) that triggers a strong shock in the surrounding rock mass. Both the kinetic energy of the block system and the dissipated energy due to
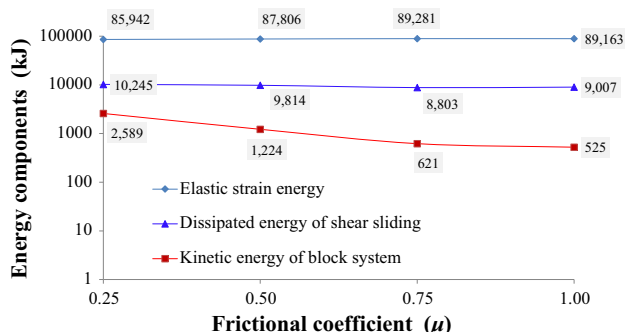
shear sliding decrease with increasing friction coefficient, as would be intuitively expected, but the elastic strain energy stored in the rock mass increases with increasing friction, which is less intuitive. The kinetic energy of the block system is the lowest among the three energy components whereas the elastic strain energy stored in the rock is much greater than both the dissipated and kinetic energy components of the block system (note that the energy axis scale is logarithmic in Fig. 13). This is because the affected area in the simulation is 36 times larger than the area of the excavation.

4.3 Influence of In Situ Stress on Rockburst Energy

To explore the role of initial stress, four cases with various initial stress magnitudes are calculated and the results are shown in Fig. 14 for a constant principal stress ratio of $k = 2$. The four maximum principal stresses ($\sigma_1 = \sigma_x$) are $30\sqrt{2}$, 60, $60\sqrt{2}$ and 120 MPa, respectively. As would be expected, all the energy components correlate well with the initial stress level. Indeed, the kinetic energy of the block system increases approximately four times from 414 kJ with $\sigma_x = 30\sqrt{2}$ MPa up to 1540 kJ with $\sigma_x = 120$ MPa.

Studying a single ejected keyblock as a result of strain relaxation (see Fig. 11c) helps facilitate the understanding of rockburst potential in discontinuous rock masses. The violent ejection of the keyblock from the immediate face of the excavation is attributed to the transfer of a small part of the kinetic energy of the block system to seismic energy. The evolution of the kinetic energy of the ejected keyblock is demonstrated in Fig. 15, taking into account four in situ stress magnitudes and a discontinuity friction angle of 45°. As would be expected, with increasing in situ stress the kinetic energy of the ejected key block increases due to the increasing release of kinetic energy of the block system in the affected area.
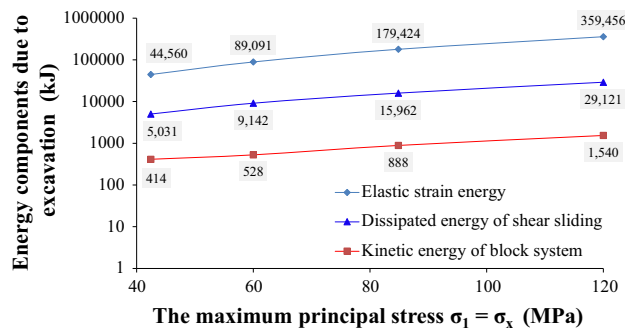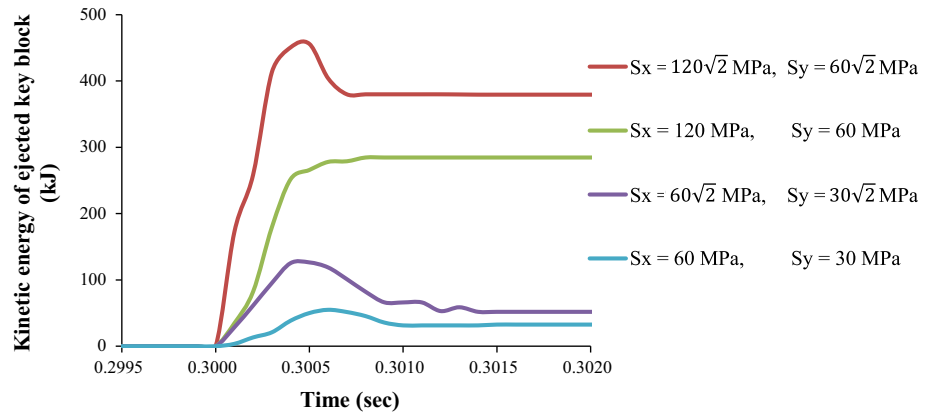

Fig. 13 Influence of frictional resistance on the three dynamic energy components of surrounding rocks after excavation (color figure online)

Fig. 14 Influence of in situ stresses magnitude on the energy components under the constant principal stress ratio $k = 2$. Note that the maximum principal stress on x-axis is referred to as σ_x; and $\sigma_y = \sigma_x/k$

Fig. 15 Evolution of kinetic energy of the ejected key block with various initial stress magnitudes, friction coefficient $\mu = 1$

5 Discussion

5.1 Relative Significance of Energy Components in Discontinuous Rocks

Once the shear stress acting on the sliding plane of a potential key block exceeds the shear strength across that plane, a seismic event will instantaneously take place in the form of shear sliding (Singh 1988). The kinetic energy of the block system that generates an instantaneous shock in the affected area can assist in gaining an insight into some of the fundamental aspects of rockbursts. In the sense of kinetics transformation, with decreasing frictional resistance of pre-existing discontinuities the sudden release of strain energy due to tunneling is increased in highly stressed environments, resulting in stronger instantaneous shock energy, thus increasing the likelihood for rockbursts; see Figs. 12 and 13. We find that the kinetic energy of the block system, considered as the intrinsic source of rockbursting, is most sensitive to frictional resistance offered by pre-existing discontinuities. The kinetic energy in the affected area drops by a factor of 5 (!) from 2589 to 525 kJ when joint friction is increased over a reasonable range for rock discontinues, from $\mu = 0.25$ to $\mu = 1.0$ (see Fig. 13).

Regarding the minor influence of friction coefficient on the dissipated energy the flowing argument may be put forth. With decreasing frictional resistance the magnitude of shear displacement increases ($d_s \uparrow$) and therefore more energy is available to be released as seismic energy together with a stronger rockburst shock. Yet, considering the Mohr–Coulomb failure criterion, with decreasing friction coefficient the shear resistance $(\sigma_n \times \mu \downarrow)$ is reduced assuming constant normal stress (σ_n) on the joints. Therefore, the dissipated energy $(\sigma_n \times \mu \downarrow \times d_s \uparrow)$ due to shear sliding is not very sensitive to the frictional resistance (refer to blue line in Fig. 13).

It should be pointed out that at the Jinping II hydro-electric project, energy levels of microseismicity based on real-time monitoring systems have been established for predicting various intensities of rockbursts defined by amplitude of acoustic emissions (Feng et al. 2012). Here, we simulated the evolution of kinetic energy of the block system in the process of rockbursts. We believe the instantaneous shock energy of the block system as computed with DDA is a good proxy for the temporal behavior of micro-seismic energy as monitored in the field. This should be an area of further research.

5.2 Mitigating Rockburst Potential by Top Heading Distressing

As discussed in previous sections, with increasing size of excavation increasing elastic strain energy will be transferred to the surrounding rock near the opening boundary, thus increasing the kinetic energy of the affected area and the potential for stronger rockbursts. In practice, when a relatively large cross sectional area is required the working face is commonly divided into several parts to be excavated sequentially, to reduce both the sudden release of strain energy as well as the instantaneous kinetic energy of the system.

During construction of the Jinping II hydropower station in China under a maximum overburden depth of 2525 m, a number of extremely intense rockbursts occurred when excavating the auxiliary and drainage tunnels. Two of the four parallel 12.4 m diameter headrace tunnels were excavated using large diameter TBMs thus significantly increasing the rockbursting potential (Zhang et al. 2012); see Fig. 16. To enable alleviating the extremely intensive

To summarize this section, we may conclude that two factors directly influence the magnitude of the kinetic energy of the block system which is a proxy for rockburst hazard: (1) frictional resistance as an internally intrinsic factor, (2) level of in situ stress as an externally driving factor.

Fig. 16 The rockburst events in the construction of the tunnel in Jinping hydropower station, China: **a** the moderate rockburst behind finger-shaped shield on March 7, 2009; **b** the intensive rockburst on the south sidewall on August 17, 2008; **c** the intensive rockburst on the north sidewall on September 12, 2008; **d** the extremely intense rockburst on November 28, 2009 (modified after Zhang et al. 2012)
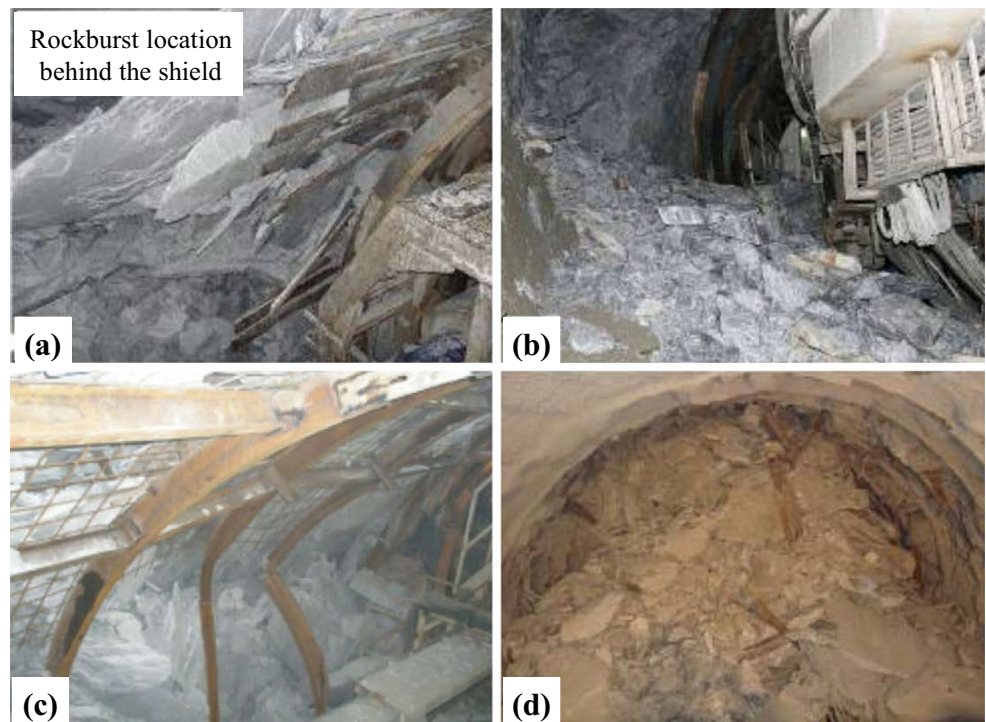

Fig. 17 Sketch map of pilot tunnels adopted in Jinping hydropower station for mitigating rockbursts (unit: m): **a** top heading with half height of tunnel; **b** upper pilot tunnel; **c** center pilot tunnel (modified after Wang et al. 2012)
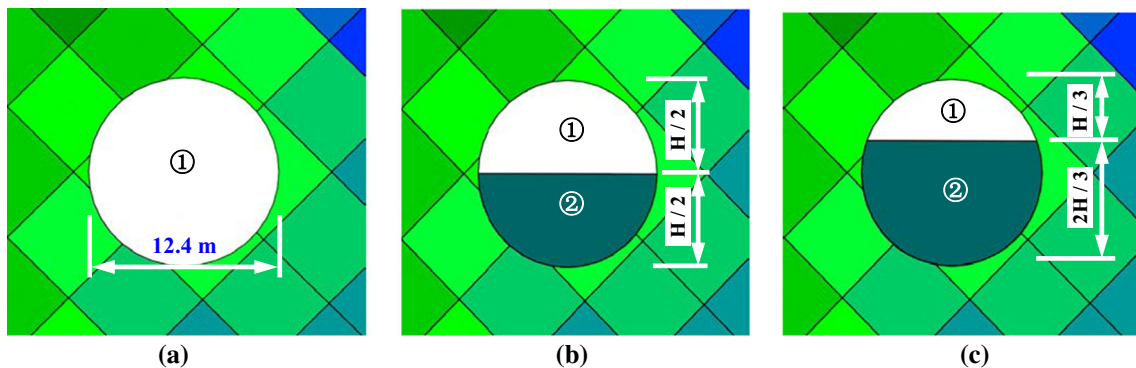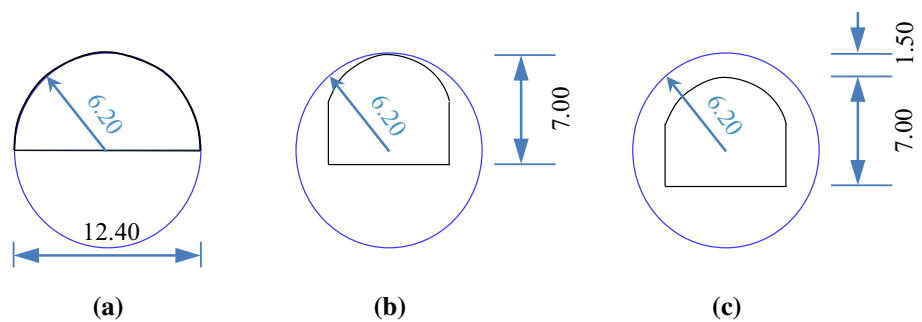

Fig. 18 Excavation sequence schemes of three scenarios (unit: m): **a** full-face excavation; **b** top heading with half height of tunnel; **c** top heading with one-third height of tunnel

rockbursts, a top heading excavation was conducted in the field (refer to Fig. 17). To study the efficiency of top heading and bench excavation methodology in alleviating rockbursting potential we model three geometries with DDA, as shown in Fig. 18. Note that the top heading of half the tunnel height (Fig. 18b) was actually applied in the

Jinping hydroelectric project to mitigate the risk of rock-bursts. Using accurate sliding micrometer data obtained during the excavation of a research tunnel within the Jin-ping tunnel complex, the in situ stress field in Jinping tunnels was obtained by inversion using the numerical manifold method (Tal et al. 2014) and the resulting stress state is shown in Fig. 19a. The material properties used in the simulations here are the values obtained in the field (Li et al. 2012): Young's modulus ($E = 25.3$ GPa) and Poisson's ratio ($v = 0.22$) and are kept constant throughout our simulations. The modeled cross section in DDA is shown in Fig. 19b. With the real span of $D = 12.4$ m as excavated in Jinping, the number of monitoring blocks in the affected area in the DDA mesh is 125.

The evolution of kinetic energy in the affected area in response to top heading and bench excavation is shown in Fig. 20 for different top heading and bench geometries. Full-face excavation (red line in Fig. 20) gives rise to the highest kinetic energy in the affected zone of 3577 kJ, triggering the strongest instantaneous shock among the three excavation scenarios. Top heading of half the height of tunnel (blue line in Fig. 20) drops the kinetic energy of the block system to 2014 kJ, a reduction of 56 %, indicating that top heading excavation can reduce the kinetic energy so as to effectively reduce the intensity of rockbursting. Excavation of the bench (at 0.40 s) results in only minor kinetic energy of the block system of 354 kJ, which is negligible during the construction.

The DDA results are in good agreement with monitored rockburst events experienced during construction of the Jinping hydroelectric project. Between August, 2008 and November, 2009, intense and extremely intense rockbursts were recorded at tunnels excavated with full-face approach (Zhang et al. 2012); see Fig. 16. On November 28, 2009,
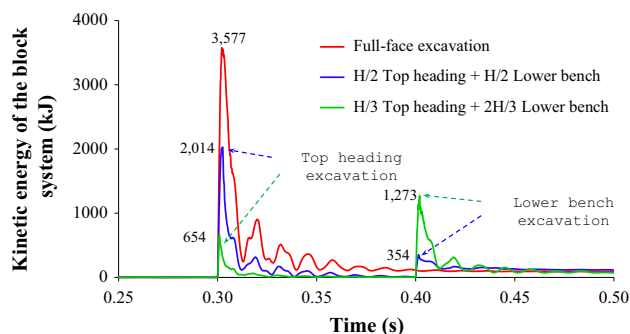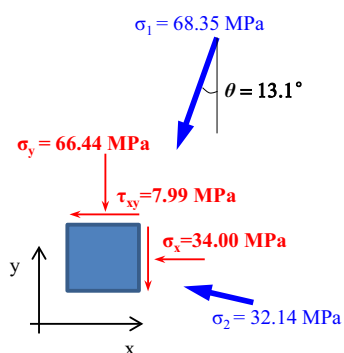

Fig. 20 Evolution of kinetic energy of the block system with three excavation schemes, i.e., full-face excavation, top headings with half height of tunnel and with one-third height of tunnel, respectively (color figure online)

an extremely intense rockburst occurred and the TBM equipment was buried along a 28 m long section. Then top heading excavation of half tunnel height was employed to distress and partly release the stored strain energy. Thereafter, neither intense nor extremely intense rockbursts were monitored when top heading of half tunnel height was utilized; all monitored rockbursts were classified as moderate when top heading excavation was utilized. Moreover, rockbursts never occurred during lower bench excavation.
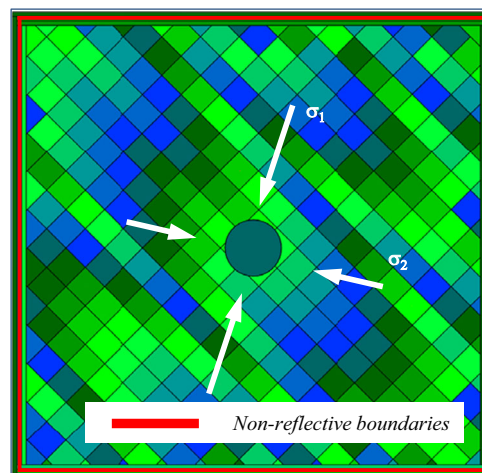
The relative height of the top heading with respect to the tunnel height is also significant. When the top heading is 1/3 the tunnel height the kinetic energy of the system drops further to 654 kJ (green line in Fig. 20), however when the bench is removed in this configuration the kinetic energy of the block system increases to 1273 kJ. The height of top heading should therefore be optimized using numerical approaches as demonstrated here.

Interestingly, similar to the top heading distressing for reducing the cross sectional area, Huang et al. (2001)

Fig. 19 Modified DDA modelling for Jinping hydroelectric station: **a** in situ stresses components; **b** the DDA model with non-reflective boundaries. Note the input in situ stress (Tal et al. 2014) obtained by coordinate transformation from principal stresses

(a)

(b)

proposed that rockbursts during tunneling could be controlled by lowering the excavation speed in the tunnel axis direction, the principle of which is the same as top heading distressing, that is, reducing the volume of one-time opening.

Finally, it should be noted that this study does not take into consideration time-dependent strength degradation of the rock mass, yet it has been shown that the long-term strength of rock mass is less than 0.7 times the short-term strength (Martin 1993). Time dependent strength degradation of the rock mass can explain why some rockbursts occur 5–20 h after the excavation is formed. Instabilities in the form of seismic events can be initiated by the smallest changes in stress if any point in the rock mass is close to unstable equilibrium. The modeling of this failure mechanism, however, is beyond the scope of this study.

6 Summary and Conclusions

- Based on theoretical and numerical analyses, we propose a new model to quantitatively calculate energy components during rockburst generation, and identify the conditions at which violent rockbursts are most likely to occur in discontinuous, relatively stiff, rock masses, with the aim of providing an in-depth understanding of the physical mechanism of rockburst generation due to strain relaxation.
- Using theoretical analysis based on linear elasticity we find that the creation of a circular opening results in initial strain energy increase by approximately 1.7 times to a distance of three diameters from the tunnel center, regardless of radius of excavation, initial principal stresses and elastic modulus of the rock. This result defines the affected area around the excavation.
- We find that an annulus thickness of half tunnel diameter from the opening boundary is expected to generate most rockbursting activity, thus defining the RPZ around the excavation. The RPZ is the effective depth to be utilized for alleviating rockbursts, by distressing boreholes, top heading excavations or rock bolting.
- The numerical discrete element DDA method is first validated using field measurements particularly with respect to radial P-wave propagation from a point source, and is then utilized to derive the energy components during rockbursts in discontinuous rock masses.
- The three dynamic energy components involved in energy transformation during rockbursting deformation: energy dissipation due to shear sliding, kinetic energy of the block system and residual strain energy stored in rock mass around excavation, are determined for a discontinuous rock system using DDA. The kinetic energy of the block system provides an insight into the mechanism of strain rockburst generation. We believe the instantaneous shock energy of the block system as computed with DDA can be used as a good proxy for temporal microseismicity monitored in the field.
- With increasing initial stresses, energy dissipation due to frictional sliding increases and so does the kinetic energy of the ejected blocks, leading to greater intensity of rockbursts. We find that with decreasing frictional resistance of pre-existing discontinuities, the sudden release of strain energy associated with tunneling is increased, thus increasing the potential for rockbursting in the RPZ.
- Top heading distressing can alleviate rockbursting energy by decreasing the instantaneous shock associated with single face boring. The effect of top heading distressing in reducing rockburst energy as modeled here with DDA is supported by field measurements performed during excavation of the Jinping hydroelectric complex. Using the numerical approach proposed here the height of the top heading with respect to the height of the excavation can be optimized.

Appendix: Analytical Solution for the Energy Change Due to Tunneling in a Continuous Rock Mass Using Linear Elasticity

To obtain the energy change due to tunneling in an infinite elastic plate consisting of isotropic material we will investigate the total elastic strain energy stored in an annulus S_B pre and post excavation (see Fig. 1).

Initial Energy in Analyzed Domain

The elastic strain energy density (ϕ) stored in a rock subjected to a three-dimensional stress field is given by:

$$\phi = \frac{1}{2}\left(\sigma_x \varepsilon_x + \sigma_y \varepsilon_y + \sigma_z \varepsilon_z + \tau_{xy}\gamma_{xy} + \tau_{yz}\gamma_{yz} + \tau_{zx}\gamma_{zx}\right) \tag{12}$$

Assuming linear elastic rock, the general form of the constitutive equation is as follows (Timoshenko and Goodier 1970):

$$\begin{cases} \varepsilon_x = \frac{1}{E}\left[\sigma_x - v(\sigma_y + \sigma_z)\right] \\ \varepsilon_y = \frac{1}{E}\left[\sigma_y - v(\sigma_x + \sigma_z)\right] \\ \varepsilon_z = \frac{1}{E}\left[\sigma_z - v(\sigma_x + \sigma_y)\right] \\ \gamma_{xy} = \frac{2(1+v)}{E}\tau_{xy}, \gamma_{yz} = \frac{2(1+v)}{E}\tau_{yz}, \gamma_{zx} = \frac{2(1+v)}{E}\tau_{zx} \end{cases}$$
(13)

Substituting Eq. (13) into Eq. (12), we can express the general solution of elastic strain energy density by stress components:

$$\phi = \frac{1}{2E}\left[\left(\sigma_x^2 + \sigma_y^2 + \sigma_z^2\right) - 2v\left(\sigma_y\sigma_z + \sigma_z\sigma_x + \sigma_x\sigma_y\right)\right.$$
$$\left. + 2(1+v)\left(\tau_{yz}^2 + \tau_{zx}^2 + \tau_{xy}^2\right)\right]$$
(14)

In the notation adopted here pre and post excavation states will be indicated by superscripts (°) and (*), respectively; for the general case no superscript is used. Assuming plane-strain, the strain parallel to the tunnel axis (Fig. 1a) is given by: $\varepsilon_z = \frac{1}{E}\left[\sigma_z^o - v(\sigma_x^o + \sigma_y^o)\right] = 0$ and therefore the axial stress is: $\sigma_z^o = v(\sigma_x^o + \sigma_y^o)$. Assuming σ_x^o, σ_y^o, and σ_z^o are principal stresses, the shear stresses in the cross-sectional planes are zero ($\tau_{yz}^o = \tau_{zx}^o = \tau_{xy}^o = 0$). It can be shown, however, that once the excavation space is created, the shear stress component $\tau_{xy}^* \neq 0$ (see "Energy Change Due to Excavation" section in Appendix), whereas $\tau_{yz}^* = \tau_{zx}^* = 0$. Substituting these stress components into Eq. (14), we obtain the elastic strain energy density expression for pre and post excavation states under plane-strain conditions:

$$\phi = \frac{1}{2E}\left\{\left(\sigma_x^2 + \sigma_y^2 + v^2(\sigma_x + \sigma_y)^2\right) - 2v\left[v\sigma_y(\sigma_x + \sigma_y)\right.\right.$$
$$\left.\left. + v(\sigma_x + \sigma_y)\sigma_x + \sigma_x\sigma_y\right] + 2(1+v)\tau_{xy}^2\right\}$$
$$= \frac{1+v}{2E}\left[(1-v)(\sigma_x + \sigma_y)^2 - 2\sigma_x\sigma_y + 2\tau_{xy}^2\right]$$
(15)

The elastic strain energy in the initial state (before excavation) can be obtained:

$$U_{A,B}^o = \int_{S_B} \phi^o dV$$
$$= \frac{1+v}{2E}\left[(1-v)(\sigma_x^o + \sigma_y^o)^2 - 2\sigma_x^o\sigma_y^o\right] \times S_{A,B}$$
(16)

The excavation-induced energy can be obtained by integrating Eq. (15) within volume element dV_B, for unit length of the tunnel under plane-strain conditions (see Fig. 1b):

$$U_B^* = \int_{S_B} \phi^* dV = \int_{S_B} \phi^* dS \times 1\text{ m}$$

$$= \frac{1+v}{2E}\left[(1-v)\int_{S_B}(\sigma_x^* + \sigma_y^*)^2 dS - 2\int_{S_B}\sigma_x^*\sigma_y^* dS + 2\int_{S_B}\tau_{xy}^{*2} dS\right]$$
(17)

where S_B is the annulus area in cross-sectional plane (see Fig. 1b).

Energy Change Due to Excavation

Let us find now the change in energy due to excavation of a circular tunnel. The stress concentrations in cylindrical coordinates around the circular tunnel can be found by direct application of the well-known Kirsch solution (Kirsch 1898):

$$\begin{cases} \sigma_r^* = \frac{\sigma_x^o + \sigma_y^o}{2}\left(1 - \frac{a^2}{r^2}\right) + \frac{\sigma_x^o - \sigma_y^o}{2}\left(1 - \frac{a^2}{r^2}\right)\left(1 - \frac{3a^2}{r^2}\right)\cos 2\theta \\ \sigma_\theta^* = \frac{\sigma_x^o + \sigma_y^o}{2}\left(1 + \frac{a^2}{r^2}\right) - \frac{\sigma_x^o - \sigma_y^o}{2}\left(1 + \frac{3a^4}{r^4}\right)\cos 2\theta \\ \tau_{r\theta}^* = -\frac{\sigma_x^o - \sigma_y^o}{2}\left(1 - \frac{a^2}{r^2}\right)\left(1 + \frac{3a^2}{r^2}\right)\sin 2\theta \end{cases}$$
(18)

To obtain the total elastic strain energy after excavation we must evaluate the three expressions in Eq. (17) ($\int_{S_B}\left(\sigma_x^* + \sigma_y^*\right)^2 dS$; $\int_{S_B}\sigma_x^*\sigma_y^* dS$; $\int_{S_B}\tau_{xy}^{*2} dS$) in terms of cylindrical coordinates so that Kirsch solution may be conveniently applied.

Deriving $\int_{S_B}\left(\sigma_x^* + \sigma_y^*\right)^2 dS$: by employing the first stress invariant and Eq. (18) we may write:

$$\sigma_x^* + \sigma_y^* = \sigma_r^* + \sigma_\theta^* = \sigma_x^o + \sigma_y^o - 2\left(\sigma_x^o - \sigma_y^o\right)\frac{a^2}{r^2}\cos 2\theta \quad (19)$$

Using Eq. (19) and integrating within annulus S_B we get:

$$\int_{S_B}\left(\sigma_x^* + \sigma_y^*\right)^2 dS = \int_a^b \int_0^{2\pi}(\sigma_x^* + \sigma_y^*)^2 r d\theta dr$$
$$= 2\pi \int_a^b \left(\sigma_x^o + \sigma_y^o\right)^2 r dr + 2\pi \int_a^b 2\left(\sigma_x^o - \sigma_y^o\right)^2 \frac{2a^4}{r^3} dr$$
(20)

Deriving $\int_{S_B}\sigma_x^*\sigma_y^* dS$: the rotation matrix from cylindrical to Cartesian coordinate systems (Fig. 21) is:

$$Q_{ij} = \begin{bmatrix} \cos\theta & -\sin\theta \\ \sin\theta & \cos\theta \end{bmatrix}$$
(21)

Employing the second-order matrix transformation of isotropic tensor from Cylindrical to Cartesian coordinate systems, we get:

$$\sigma^*(x,y) = Q_{ij} \times \sigma^*(r,\theta) \times Q_{ij}^T$$

$$\begin{bmatrix} \sigma_x^* & \tau_{xy}^* \\ \tau_{yx}^* & \sigma_y^* \end{bmatrix} = \begin{bmatrix} \cos\theta & -\sin\theta \\ \sin\theta & \cos\theta \end{bmatrix} \begin{bmatrix} \sigma_r^* & \tau_{r\theta}^* \\ \tau_{\theta r}^* & \sigma_\theta^* \end{bmatrix} \begin{bmatrix} \cos\theta & -\sin\theta \\ \sin\theta & \cos\theta \end{bmatrix}^T$$

$$= \begin{bmatrix} \cos\theta\sigma_r^* - \sin\theta\tau_{r\theta}^* & \cos\theta\tau_{r\theta}^* - \sin\theta\sigma_\theta^* \\ \sin\theta\sigma_r^* + \cos\theta\tau_{\theta r}^* & \sin\theta\tau_{r\theta}^* + \cos\theta\sigma_\theta^* \end{bmatrix}$$

$$\times \begin{bmatrix} \cos\theta & \sin\theta \\ -\sin\theta & \cos\theta \end{bmatrix} \tag{22}$$

Using Eq. (22) the stress components (σ_x^*, σ_y^*, τ_{xy}^*) after the excavation in terms of cylindrical coordinate are:

$$\begin{cases} \sigma_x^* = \cos^2\theta\sigma_r^* - \sin 2\theta\tau_{r\theta}^* + \sin^2\theta\sigma_\theta^* \\ \sigma_y^* = \sin^2\theta\sigma_r^* + \sin 2\theta\tau_{r\theta}^* + \cos^2\theta\sigma_\theta^* \\ \tau_{xy}^* = \frac{1}{2}\sin 2\theta(\sigma_r^* - \sigma_\theta^*) + \cos 2\theta\tau_{r\theta}^* \end{cases} \tag{23}$$

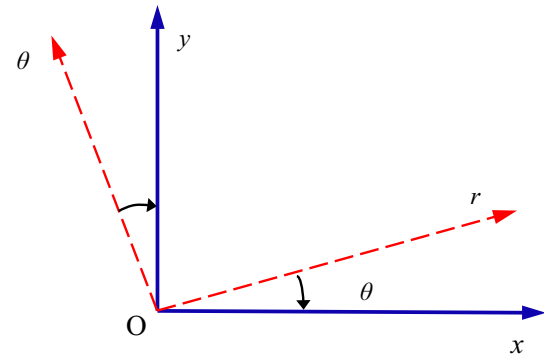and therefore the magnitude of the term $\sigma_x^*\sigma_y^*$ at every point around the circular opening is:

Fig. 21 Second order tensor coordination transformation

$$\sigma_x^*\sigma_y^* = \frac{1}{8}(1 - \cos 4\theta)\sigma_r^{*2} + \frac{1}{2}\sin 4\theta\sigma_r^*\tau_{r\theta}^*$$
$$+ \left(\frac{3 + \cos 4\theta}{4}\right)\sigma_\theta^*\sigma_r^* + \frac{\cos 4\theta - 1}{2}\tau_{r\theta}^{*2}$$
$$- \frac{1}{2}\sin 4\theta\sigma_\theta^*\tau_{r\theta}^* + \frac{1}{8}(1 - \cos 4\theta)\sigma_\theta^{*2} \tag{24}$$

The six components of Eq. (24) are:

$$\sigma_x^*\sigma_y^* = \left[\cos^2\theta\sigma_r^* - \sin 2\theta\tau_{r\theta}^* + \sin\theta^2\sigma_\theta^*\right] \times \left[\sin^2\theta\sigma_r^* + \sin 2\theta\tau_{r\theta}^* + \cos^2\theta\sigma_\theta^*\right]$$

$$= \cos^2\theta\sin^2\theta\sigma_r^{*2} + \sin 2\theta\cos^2\theta\sigma_r^*\tau_{r\theta}^* + \cos^4\theta\sigma_\theta^*\sigma_r^* - \sin^2\theta\sin 2\theta\sigma_r^*\tau_{r\theta}^* - \sin^2 2\theta\tau_{r\theta}^{*2}$$

$$- \sin 2\theta\cos^2\theta\sigma_\theta^*\tau_{r\theta}^* + \sin^4\theta\sigma_\theta^*\sigma_r^* + \sin 2\theta\sin^2\theta\sigma_\theta^*\tau_{r\theta}^* + \cos^2\theta\sin^2\theta\sigma_\theta^{*2}$$

$$= \underbrace{\frac{1}{8}(1 - \cos 4\theta)\sigma_r^{*2}}_{①} + \underbrace{\frac{1}{2}\sin 4\theta\sigma_r^*\tau_{r\theta}^*}_{②} + \underbrace{\left(1 - \frac{1 - \cos 4\theta}{4}\right)\sigma_\theta^*\sigma_r^*}_{③} + \underbrace{\frac{\cos 4\theta - 1}{2}\tau_{r\theta}^{*2}}_{④} \tag{25}$$

$$\underbrace{- \frac{1}{2}\sin 4\theta\sigma_\theta^*\tau_{r\theta}^*}_{⑤} + \underbrace{\frac{1}{8}(1 - \cos 4\theta)\sigma_\theta^{*2}}_{⑥}$$

From application of Kirsch solution the term σ_r^{*2} is:

$$\sigma_r^{*2} = \left(\frac{\sigma_x^o + \sigma_y^o}{2}\right)^2\left(1 - \frac{a^2}{r^2}\right)^2 + \left(\frac{\sigma_x^o - \sigma_y^o}{2}\right)^2\left(1 - \frac{a^2}{r^2}\right)^2\left(1 - \frac{3a^2}{r^2}\right)^2\frac{1 + \cos 4\theta}{2} + \frac{\sigma_x^{o2} - \sigma_y^{o2}}{2}\left(1 - \frac{a^2}{r^2}\right)^2\left(1 - \frac{3a^2}{r^2}\right)\cos 2\theta$$

$$① = \frac{1}{8}(1 - \cos 4\theta)\sigma_r^{*2} = \underbrace{\frac{1}{8}\sigma_r^{*2}}_{A1} - \underbrace{\frac{1}{8}\cos 4\theta\sigma_r^{*2}}_{B1} \quad \text{and therefore:}$$

$$A1 = \frac{1}{8}\left[\left(\frac{\sigma_x^o + \sigma_y^o}{2}\right)^2\left(1 - \frac{a^2}{r^2}\right)^2 + \left(\frac{\sigma_x^o - \sigma_y^o}{2}\right)^2\left(1 - \frac{a^2}{r^2}\right)^2\right.$$
$$\left.\left(1 - \frac{3a^2}{r^2}\right)^2\frac{1 + \cos 4\theta}{2} + \frac{\sigma_x^{o2} - \sigma_y^{o2}}{2}\left(1 - \frac{a^2}{r^2}\right)^2\left(1 - \frac{3a^2}{r^2}\right)\cos 2\theta\right]$$

$$(26)$$

Since $\int_0^{2\pi}\sin n\theta \mathrm{d}\theta = \frac{1}{n}\cos n\theta|_0^{2\pi} = 0 = \int_0^{2\pi}\cos n\theta \mathrm{d}\theta$, the following terms in term $A1$ of Eq. (26), must all equal zero:

$$\int_a^r\int_0^{2\pi}\left(\frac{\sigma_x^o - \sigma_y^o}{2}\right)^2\left(1 - \frac{a^2}{r^2}\right)^2\left(1 - \frac{3a^2}{r^2}\right)^2\frac{\cos 4\theta}{2}r\mathrm{d}\theta\mathrm{d}r$$
$$= \int_a^r\left(\int_0^{2\pi}\frac{\cos 4\theta}{2}\mathrm{d}\theta\right)\left(\frac{\sigma_x^o - \sigma_y^o}{2}\right)^2\left(1 - \frac{a^2}{r^2}\right)^2\left(1 - \frac{3a^2}{r^2}\right)^2 r\mathrm{d}r$$
$$= \int_a^r\int_0^{2\pi}\frac{\sigma_x^{o2} - \sigma_y^{o2}}{2}\left(1 - \frac{a^2}{r^2}\right)^2\left(1 - \frac{3a^2}{r^2}\right)\cos 2\theta r\mathrm{d}\theta\mathrm{d}r$$
$$= 0$$

After deleting the terms containing the expression $\cos n\theta$ we obtain $\int_a^b\int_0^{2\pi}A1 \times r\mathrm{d}\theta\mathrm{d}r = \int_a^b\int_0^{2\pi}A1' \times r\mathrm{d}\theta\mathrm{d}r$, where $A1'$ is $A1$ after deleting the terms containing $\cos n\theta$. Substituting Eq. (25) into $\int \sigma_x^*\sigma_y^*\mathrm{d}A_{xy}$ using integration, we get:

$$\int_a^b\int_0^{2\pi}\sigma_x^*\sigma_y^* r\mathrm{d}\theta\mathrm{d}r = \int_a^b\int_0^{2\pi}(①+②+③+④+⑤+⑥)r\mathrm{d}\theta\mathrm{d}r$$
$$= \int_a^b\int_0^{2\pi}(①'+②'+③'+④'+⑤'+⑥')r\mathrm{d}\theta\mathrm{d}r$$

$$(27)$$

Similarly, after removing the terms containing the expression $\cos n\theta$, $A1'$ and $B1'$ can be written as:

$$A1' = \frac{1}{8}\left[\left(\frac{\sigma_x^o + \sigma_y^o}{2}\right)^2\left(1 - \frac{a^2}{r^2}\right)^2 + \left(\frac{\sigma_x^o - \sigma_y^o}{2}\right)^2\right.$$
$$\left.\times\left(1 - \frac{a^2}{r^2}\right)^2\left(1 - \frac{3a^2}{r^2}\right)^2\frac{1}{2}\right]$$

$$B1' = -\frac{1}{8}\frac{\left(\sigma_x^o - \sigma_y^o\right)^2}{16}\left(1 - \frac{a^2}{r^2}\right)^2\left(1 - \frac{3a^2}{r^2}\right)^2$$

The first component ①' is:

$$①' = A1' + B1' = \frac{\left(\sigma_x^o + \sigma_y^o\right)^2}{32}\left(1 - \frac{a^2}{r^2}\right)^2 + \frac{\left(\sigma_x^o - \sigma_y^o\right)^2}{128}\left(1 - \frac{a^2}{r^2}\right)^2\left(1 - \frac{3a^2}{r^2}\right)^2$$
$$= \frac{\left(\sigma_x^o + \sigma_y^o\right)^2}{32}\left(1 - \frac{2a^2}{r^2} + \frac{a^4}{r^4}\right) + \frac{\left(\sigma_x^o - \sigma_y^o\right)^2}{128}\left(1 - \frac{8a^2}{r^2} + \frac{22a^4}{r^4} - \frac{24a^6}{r^6} + \frac{9a^8}{r^8}\right)$$

$$(28)$$

In the same manner as above, after deleting all terms containing the expression $\cos n\theta$ the remaining five components of Eq. (27) can be expressed as:

$$②' = -\frac{\left(\sigma_x^o - \sigma_y^o\right)^2}{32}\left(1 - \frac{a^2}{r^2}\right)^2\left(1 - \frac{9a^4}{r^4}\right) = -\frac{\left(\sigma_x^o - \sigma_y^o\right)^2}{32}\left(1 - \frac{2a^2}{r^2} - \frac{8a^4}{r^4} + \frac{18a^6}{r^6} - \frac{9a^8}{r^8}\right)$$

$$③' = \frac{3\left(\sigma_x^o + \sigma_y^o\right)^2}{16}\left(1 - \frac{a^4}{r^4}\right) - \frac{7\left(\sigma_x^o - \sigma_y^o\right)^2}{64}\left(1 - \frac{a^2}{r^2}\right)\left(1 - \frac{3a^2}{r^2}\right)\left(1 + \frac{3a^4}{r^4}\right)$$

$$= \frac{3\left(\sigma_x^o + \sigma_y^o\right)^2}{16}\left(1 - \frac{a^4}{r^4}\right) - \frac{7\left(\sigma_x^o - \sigma_y^o\right)^2}{64}\left(1 - \frac{4a^2}{r^2} + \frac{6a^4}{r^4} - \frac{12a^6}{r^6} + \frac{9a^8}{r^8}\right)$$

$$④' = -\frac{3\left(\sigma_x^o - \sigma_y^o\right)^2}{32}\left(1 + \frac{3a^2}{r^2}\right)^2\left(1 - \frac{a^2}{r^2}\right)^2 = -\frac{3\left(\sigma_x^o - \sigma_y^o\right)^2}{32}\left(1 + \frac{4a^2}{r^2} - \frac{2a^4}{r^4} - \frac{12a^6}{r^6} + \frac{9a^8}{r^8}\right)$$

$$⑤' = -\frac{\left(\sigma_x^o - \sigma_y^o\right)^2}{32}\left(1 + \frac{3a^2}{r^2}\right)\left(1 - \frac{a^2}{r^2}\right)\left(1 + \frac{3a^4}{r^4}\right) = -\frac{\left(\sigma_x^o - \sigma_y^o\right)^2}{32}\left(1 + \frac{2a^2}{r^2} + \frac{6a^6}{r^6} - \frac{9a^8}{r^8}\right)$$

$$⑥' = \frac{\left(\sigma_x^o + \sigma_y^o\right)^2}{32}\left(1 + \frac{a^2}{r^2}\right)^2 + \frac{\left(\sigma_x^o - \sigma_y^o\right)^2}{128}\left(1 + \frac{3a^4}{r^4}\right)^2$$

$$= \frac{\left(\sigma_x^o + \sigma_y^o\right)^2}{32}\left(1 + \frac{2a^2}{r^2} + \frac{a^4}{r^4}\right) + \frac{\left(\sigma_x^o - \sigma_y^o\right)^2}{128}\left(1 + \frac{6a^4}{r^4} + \frac{9a^8}{r^8}\right)$$

(29)

Adding up all the components after deleting the zero terms we get:

$$①' + ②' + ③' + ④' + ⑤' + ⑥' = \sigma_x^o\sigma_y^o - \frac{\left(\sigma_x^o + \sigma_y^o\right)^2}{8}\frac{a^4}{r^4} + \frac{3\overline{\left(\sigma_x^o - \sigma_y^o\right)^2}}{2}\frac{a^6}{r^6} - \frac{9\left(\sigma_x^o - \sigma_y^o\right)^2}{8}\frac{a^8}{r^8}$$

(30)

Substituting Eq. (30) into $\int \sigma_x^*\sigma_y^* dS$ we can integrate the annulus domain S_B:

$$\int_{S_B} \sigma_x^*\sigma_y^* dS = \int_a^b\int_0^{2\pi} \sigma_x^*\sigma_y^* r\,d\theta dr = \int_a^b\int_0^{2\pi}\left(①' + ②' + ③' + ④' + ⑤' + ⑥'\right)r\,d\theta dr$$

$$= 2\pi\int_a^b \sigma_x^o\sigma_y^o r - \frac{\left(\sigma_x^o + \sigma_y^o\right)^2}{8}\frac{a^4}{r^3} + \frac{3\left(\sigma_x^o - \sigma_y^o\right)^2}{2}\frac{a^6}{r^5} - \frac{9\left(\sigma_x^o - \sigma_y^o\right)^2}{8}\frac{a^8}{r^7}dr$$

(31)

Deriving $\int_{S_B} \tau_{xy}^{*2}\mathrm{d}S$: substituting Eq. (18) into the expression for τ_{xy}^* in Eq. (23), we obtain the excavation-induced shear stress:

$$\tau_{xy}^* = -\frac{\sigma_x^o + \sigma_y^o}{2}\frac{a^2}{r^2}\sin 2\theta - \frac{\sigma_x^o - \sigma_y^o}{2}\left(\frac{2a^2}{r^2} - \frac{3a^4}{r^4}\right)\sin 4\theta$$
(32)

Note that Eq. (32) confirms that the shear stress component τ_{xy}^* is no longer zero after the excavation has been created. Recalling that $\int_0^{2\pi}\sin n\theta\,\mathrm{d}\theta = 0 = \int_0^{2\pi}\cos n\theta\,\mathrm{d}\theta$, we obtain:

$$\int_{S_B} \tau_{xy}^{*2}\mathrm{d}S = \int_a^b \int_0^{2\pi} \tau_{xy}^{*2} r\,\mathrm{d}\theta\,\mathrm{d}r = 2\pi\int_a^b \frac{\left(\sigma_x^o+\sigma_y^o\right)^2}{8}\frac{a^4}{r^3}$$
$$+ \frac{\left(\sigma_x^o-\sigma_y^o\right)^2 a^4}{8}\left(\frac{4}{r^3} - \frac{12a^2}{r^5} + \frac{9a^4}{r^7}\right)\mathrm{d}r$$
(33)

To get the total elastic strain energy stored in an annulus S_B around a circular opening after excavation (see Fig. 2), we substitute Eqs. (20), (31) and (33) into Eq. (17):

$$U_B^* = \frac{\pi}{E}\left\{(1-v^2)\int_a^b\left[\left(\sigma_x^o+\sigma_y^o\right)^2 r + 2\left(\sigma_x^o-\sigma_y^o\right)^2\frac{a^4}{r^3}\right]\mathrm{d}r\right.$$
$$+ 2(1+v)\int_a^b\left[\frac{\left(\sigma_x^o+\sigma_y^o\right)^2}{4}\frac{a^4}{r^3} + \frac{\left(\sigma_x^o-\sigma_y^o\right)^2 a^4}{4}\right.$$
$$\times\left(\frac{2}{r^3} - \frac{12a^2}{r^5} + \frac{9a^4}{r^7}\right) - \sigma_x^o\sigma_y^o r\mathrm{d}r\Big]\Big\}$$
$$= \frac{\pi}{E}\left\{(1-v^2)\left[\frac{1}{2}\left(\sigma_x^o+\sigma_y^o\right)^2 r^2\Big|_a^b - \left(\sigma_x^o-\sigma_y^o\right)^2 a^4\frac{1}{r^2}\Big|_a^b\right]\right\}$$
$$+ 2(1+v)\left[-\frac{\left(\sigma_x^o+\sigma_y^o\right)^2}{8}a^4\frac{1}{r^2}\Big|_a^b + \frac{\left(\sigma_x^o-\sigma_y^o\right)^2 a^4}{4}\right.$$
$$\times\left(-\frac{1}{r^2}\Big|_a^b + 3a^2\frac{1}{r^4}\Big|_a^b - \frac{3}{2}a^4\frac{1}{r^6}\Big|_a^b\right) - \frac{\sigma_x^o\sigma_y^o}{2}r^2\Big|_a^b$$
(34)

to obtain the total energy after the excavation in annulus S_B.

References

Bao HR, Hatzor YH, Huang X (2012) A new viscous boundary condition in the two-dimensional discontinuous deformation analysis method for wave propagation problems. Rock Mech Rock Eng 45(5):919–928

Bao HR, Yagoda-Biran G, Hatzor YH (2014) Site response analysis with two-dimensional numerical discontinuous deformation analysis method. Earthq Eng Struct D 43(2):225–246

Brady BHG, Brown ET (2006) Rock mechanics for underground mining, 3rd edn. Springer, Dordrecht

Brady BT, Leighton FW (1977) Seismicity anomaly prior to a moderate rock burst: a case study. Int J Rock Mech Min Sci 14(3):127–132

Cai M, Kaiser PK, Tasaka Y, Maejima T, Morioka H, Minami M (2004) Generalized crack initiation and crack damage stress thresholds of brittle rock masses near underground excavations. Int J Rock Mech Min Sci 41(5):833–847

Cook NGW (1966) The basic mechanics of rockbursts. J South Afr Inst Min Metall 66:56–70

Drake J, Twisdale L, Frank R, Dass W (1989) Protective construction design manual. US Air Force Engineering Service Center, Engineering and Services Laboratory, Tindall Air Force Base

Durrheim RJ, Haile A, Roberts MKC, Schweitzer JK, Spottiswoode SM, Klokow JW (1998) Violent failure of a remnant in a deep South African gold mine. Tectonophysics 289(1–3):105–116

Feng XT, Chen BG, Li SJ, Zhang CQ, Xiao YX, Feng GL, Ming HJ (2012) Studies on the evolution process of rockbursts in deep tunnels. J Rock Mech Geotech Eng 4(4):289–295

Feng GL, Feng XT, Chen BR, Xiao YX, Jiang Q (2015) Sectional velocity model for microseismic source location in tunnels. Tunn Undergr Sp Technol 45:73–83

Gu R, Ozbay U (2014) Distinct element analysis of unstable shear failure of rock discontinuities in underground mining conditions. Int J Rock Mech Min Sci 68:44–54

Hatzor YH, Feng XT, Li SJ, Yagoda-Biran G, Jiang Q, Hu LX (2015) Tunnel reinforcement in columnar jointed basalts: the role of rock mass anisotropy. Tunn Undergr Sp Technol 46:1–11

He MC, Sousa LR, Miranda T, Zhu GL (2015) Rockburst laboratory tests database—application of data mining techniques. Eng Geol 185:116–130

Heal DP (2010) Observations and analysis of incidences of rockburst damage in underground mines. Ph.D. Thesis, The University of Western Australia, Perth, Australia

Huang RQ, Wang XN, Chan LS (2001) Triaxial unloading test of rocks and its implication for rock burst. Bull Eng Geol Environ 60(1):37–41

Jiang Q, Feng XT, Xiang TB, Su GS (2010) Rockburst characteristics and numerical simulation based on a new energy index: a case study of a tunnel at 2,500 m depth. Bull Eng Geol Environ 69(3):381–388

Kaiser PK, Maloney SM (1997) Scaling laws for the design of rock support. Pure appl Geophys 150(3–4):415–434

Kaiser PK, McCreath DR, Tannant DD (1996) Canadian rockburst support handbook. Geomechanics Research Centre, Laurentian University, Sudbury

Kirsch EG (1898) Die Theorie der Elastizität und die Bedürfnisse der Festigkeitslehre. Zeitschrift Des Vereines Deutscher Ingenieure 42(28):797–807

Li SJ, Feng XT, Li ZH, Chen BR, Zhang CQ, Zhou H (2012) In situ monitoring of rockburst nucleation and evolution in the deeply buried tunnels of Jinping II hydropower station. Eng Geol 137–138:85–96

Lu CP, Dou LM, Zhang N, Xue JH, Wang XN, Liu H, Zhang JW (2013) Microseismic frequency-spectrum evolutionary rule of rockburst triggered by roof fall. Int J Rock Mech Min Sci 64:6–16

Martin C (1993) The strength of massive Lac du Bonnet granite around underground openings. Ph.D. Thesis, University of Manitoba, Winnipeg, Canada

Mitri H (1999) FE modelling of mining-induced energy release and storage rates. J South Afr Inst Min Metall 99(2):103–110

Müller W (1991) Numerical simulation of rock bursts. Min Sci Technol 12(1):27–42

Ortlepp WD, Stacey TR (1994) Rockburst mechanisms in tunnels and shafts. Tunn Undergr Sp Technol 9(1):59–65

Panthi KK (2012) Evaluation of rock bursting phenomena in a tunnel in the Himalayas. Bull Eng Geol Environ 71(4):761–769

Salamon MDG (1984) Energy considerations in rock mechanics: fundamental results. J South Afr Inst Min Metall 84(8):233–246

Shan ZG, Yan P (2010) Management of rock bursts during excavation of the deep tunnels in Jinping II Hydropower Station. Bull Eng Geol Environ 69(3):353–363

Sharan SK (2007) A finite element perturbation method for the prediction of rockburst. Comput Struct 85(17–18):1304–1309

Shi GH (1988) Discontinuous deformation analysis: a new numerical model for the statics and dynamics of block systems. Ph.D. Thesis, University of California, Berkeley, USA

Shi GH (1993) Block system modeling by discontinuous deformation analysis. Computational Mechanics, Southampton

Singh SP (1988) Burst energy release index. Rock Mech Rock Eng 21(2):149–155

Srinivasan C, Arora SK, Yaji RK (1997) Use of mining and seismological parameters as premonitors of rockbursts. Int J Rock Mech Min Sci 34(6):1001–1008

Tal Y, Hatzor YH, Feng XT (2014) An improved numerical manifold method for simulation of sequential excavation in fractured rocks. Int J Rock Mech Min Sci 65:116–128

Tang CA, Kaiser PK (1998) Numerical simulation of cumulative damage and seismic energy release during brittle rock failure—part I: fundamentals. Int J Rock Mech Min Sci 35(2):113–121

Timoshenko SP, Goodier JN (1970) Theory of elasticity, 3rd edn. McGraw-Hill, New York

Walsh JB (1977) Energy changes due to mining. Int J Rock Mech Min 14(1):25–33

Wang J, Zeng X, Zhou J (2012) Practices on rockburst prevention and control in headrace tunnels of Jinping II hydropower station. Int J Rock Mech Min Sci 3:258–268

Wu SY, Shen M, Wang J (2010) Jinping hydropower project: main technical issues on engineering geology and rock mechanics. Bull Eng Geol Environ 69(3):325–332

Xu NW, Li TB, Dai F, Zhang R, Tang CA, Tang LX (2015) Microseismic monitoring of strainburst activities in deep tunnels at the Jinping II hydropower station, China. Rock Mech Rock Eng 48(4):1434–1453

Zelig R, Hatzor YH, Feng XT (2015) Rock-burst simulations with 2D-DDA. In: Proceedings, 49th US rock mechanics/geomechanics symposium. San Francisco, USA

Zhang CQ, Feng XT, Zhou H, Qiu SL, Wu WP (2012) A top pilot tunnel preconditioning method for the prevention of extremely intense rockbursts in deep tunnels excavated by TBMs. Rock Mech Rock Eng 45(3):288–309

Zhao XG, Wang J, Cai M, Cheng C, Ma LK, Su R, Li DJ (2014) Influence of unloading rate on the strainburst characteristics of beishan granite under true-triaxial unloading conditions. Rock Mech Rock Eng 47(2):467–483

Zhu WC, Li ZH, Zhu L, Tang CA (2010) Numerical simulation on rockburst of underground opening triggered by dynamic disturbance. Tunn Undergr Sp Technol 25(5):587–599

Zubelewicz A, Mróz Z (1983) Numerical simulation of rock burst processes treated as problems of dynamic instability. Rock Mech Rock Eng 16(4):253–274